Title
Emerging Technologies and Applications of Parallel, Electrokinetic Micro and Nano Assembly

Author
Michaels, Matthew

Publication Date
2022

UNIVERSITY OF CALIFORNIA,
IRVINE

Emerging Technologies and Applications of Parallel, Electrokinetic Micro and Nano Assembly

THESIS

submitted in partial satisfaction of the requirements
for the degree of

MASTER OF SCIENCE

in Engineering

by

Matthew Ian Michaels

Thesis Committee:
Professor Lorenzo Valdevit, *Committee Chair*
Adjunct Professor Lawrence Kulinsky, *Committee Member*
Distinguished Professor Diran Apelian, *Committee Member*

2022

DEDICATION

This thesis is dedicated to the incredible women who together form the strongest and most treasured support system I have; without which, this work, nor most of my accomplishments would have been possible.

To my loving mothers Marcia and Grace: for your enthusiastic encouragement, immeasurable patience, gentle guidance, and for everything you've done to support and carry me to this point, I cannot express enough my gratitude and appreciation.

To my beautiful and brilliant wife Talia, who serves as an endless source of motivation and comfort: this work would not be possible without the support you've provided and sacrifices you've made these past few years. For that I am grateful beyond words. Much like the pursuit of scientific endeavors is driven by curiosity and passion, the energy and excitement you bring to our lives is my greatest source of inspiration and something I am so very fortunate to have.

TABLE OF CONTENTS

LIST OF FIGURES

LIST OF TABLES

List of Equations

ACKNOWLEDGMENTS

I would like to express my utmost appreciation to my thesis committee members including the committee chair Professor Lorenzo Valdevit, Professor Lawrence Kulinsky, and Professor Diran Apelian. The members of my committee not only represent some of the most knowledgeable and experienced faculty I've had the pleasure of working with, but also the most caring and dedicated individuals who have made my graduate studies meaningful and enjoyable.

I would like to extend an additional thank you to Professor Kulinsky for serving as my research adviser over these past few years. Your excitement and passion for micro manufacturing and scientific research as a whole is contagious and I am so fortunate to have had the opportunity to share in this with you.

A thank you as well to my colleagues, collaborators, and co-authors without whom this research would not have been possible, including Tuo Zhou, Shih-Yuan Yu, Fangzhou Du, and John Golden. A special thank you to Professor Muhammad Al Farque for serving as a co-advisor on portions of this research.

Lastly, I would like to acknowledge and thank the National Science Foundation for their generous financial support for this research through NSF grant CMMI-1661877.

ABSTRACT OF THE THESIS

Emerging Technologies and Applications of Parallel, Electrokinetic, Micro and Nano Assembly

By

Matthew I. Michaels

Master of Science in Engineering

University of California, Irvine, 2022

Professor Lorenzo Valdevit, Chair

As research into miniaturization continues to aid in the advancement of modern technology and engineering, increased importance has been placed on the development of micro and nano assembly techniques which are economically and commercially viable. This thesis presents novel research into the use of electrokinetically driven parallel assembly techniques of micro and nano objects. A new process for the repair of microelectrodes is reported. Through dielectrophoresis-driven parallel assembly of carbon nanotubes into conductive bridges, the process was successfully restored conductivity was successfully across fractured microelectrodes. Additionally, complete carbon nanotube structures were assembled across electrode gaps of over 170 microns, to the author's knowledge the largest reported to date. This research serves as a strong proof of concept of the capabilities and utility of parallel micro assembly techniques driven by electrokinetic forces to solve technical challenges in a quick and cost effective manner.

Additional research contained in this thesis presents a novel artificial intelligence-driven cyber-physical system, designed and built to aid in the characterization of electrokinetic forces and the response of micro objects to them. Foregoing complex calculation and modeling, the presented system was found capable of characterizing the response of polystyrene beads to changes in dielectrophoretic force

resulting from varying frequency of an induced electric field. This system demonstrates the power of integrating emerging artificial intelligence technology into micro assembly research and development. The phenomenological approach to micro assembly made possible by artificial intelligence opens up a new and exciting pathway for development of next-generation micro assembly technologies.

Chapter 1 - Introduction

1.1 Miniaturization

Miniaturization refers to the process of designing and fabricating systems, components, and technologies at increasingly smaller length scales [1]. Since its beginnings in the mid-twentieth century [1], miniaturization has served as a foundational tool to enable the rapid development of new technologies in a wide array of fields, from medicine and biotechnology, to engineering and telecommunications [1]. The history of miniaturization, however, is inexorably linked to the creation and development of the semiconductor transistor -- a technology that, through miniaturization, would become the building block of the modern digital era [2-3]. The semiconductor-based transistor used in most modern day electronics was discovered by John Bardeen and Walter Brattain at Bell Labs in 1947 [2-3]. The transistor presented considerable advantages to the vacuum tube technology it would eventually replace. Primary among these advantages was the transistor's size. Transistors could be manufactured significantly smaller than vacuum tubes, which allowed for higher transistor density in a smaller footprint and easier integration into electronic circuits [2-3]. In the many decades since the invention of the modern transistor, research has placed a strong focus on the continued miniaturization of the transistor and other similar electronic components r to create more powerful and robust technologies, such as the computers and smart phones of today. However, the focus on miniaturization was not solely isolated to the semiconductor and computing industry. Research across a variety of industries quickly began to focus on the ability to miniaturize, including medicine, optics, metrology, and many more. Today, micro-electrical-mechanical-systems (MEMS) are commonly used in a variety of applications thanks to the miniaturization efforts of the last few decades [4].

The ability to miniaturize a system or device provides considerable advantages that can improve the performance and reliability of the device while also dramatically reducing its cost. As devices become smaller, they operate more quickly and consume less power. Additionally, components, such as microsensors, benefit from increased sensitivity and selectivity on the micro scale. From a logistical point of view, micro devices take up less space and can often be multiplexed to provide for redundancies, improving the longevity and reliability of devices. Furthermore, miniaturization reduces the amount of material required to fabricate a device, leading not only to reduced costs but less waste as well [5-7]. Given the considerable challenges facing our society today, such as climate change and dwindling natural resources, the ability to create miniaturized devices that require less material, operate more efficiently, and last longer is of critical importance now more than ever.

1.2 Micromanufacturing

Micromanufacturing is, as the name implies, a term that describes the various fabrication techniques and technologies used to produce components and devices in the micro and nano domains. Micromanufacturing is the foundation of miniaturization efforts and is often the limiting factor when it comes to how small a component can be made [8].

There are many different types of micromanufacturing techniques in use today. For example, in the semiconductor and microchip industry, photolithography, a method that utilizes light sensitive photoresist materials, is a common process used to create computer microchips [8-10]. In the medical device industry, micromachining, micro-molding, and micro-electro-discharge (Micro-EDM) are common processes used to create micro and nano scale medical products [8-10].

Micromanufacturing also encompasses the field of micro assembly, the assembly of various micro components into specific structures. The most widely used micro assembly techniques today are serial assembly methods. Serial assembly refers to the manipulation and combining of components one at a time [11]. In micromanufacturing, serial assembly is most often carried out using a microgripper, miniaturized forceps capable of grabbing, moving, and releasing components at the micro length scale. Due to the nature of their use, these techniques are commonly referred to as pick-and-place assembly methods [12].

While this method of micro assembly is fairly simple, significant research has been conducted over the past few decades to improve the design of micro grippers to increase their accuracy, reliability, and the resolution the of the micro assemblies they are able to produce. For example, research into this field has produced a wide variety of different micro gripper actuation mechanisms including piezoelectric actuation [13], electrostatic actuation [14], and even shape memory alloys as a means of actuation [15]. Researchers have also developed micro gripper systems with better sensitivity. For example, a Swiss research team integrated microscale force sensors into a micro gripper system paired with an ultrasonic device used to align small biological cells prior to assembly using the gripper to assemble more delicate biological materials [16]. Further yet, some research has focused on finding alternatives to mechanical gripping of parts, opting instead for force-based methods such as capillary force micro grippers [17]. Lastly, advancements in robotics have been combined with micro grippers to created automated serial assembly systems designed to improve repeatability and precision [18-19].

Despite these developments, pick-and-place techniques, and serial assembly methods in general, suffer from a number of critical disadvantages. Firstly, serial assembly techniques are relatively slow, leading to low throughput yields and higher manufacturing costs. This slow speed often places limitation on how many micro components can be assembled before the process becomes commercially unviable. For this reason, serial assembly techniques are generally unsuitable for most industrial scale manufacturing applications. Additionally, techniques that rely on micro gripper-like tools require increasingly smaller tools to improve the resolution they can achieve. This highlights an important limitation, as the further miniaturization of a device requires subsequent miniaturization of the tools used to fabricate it.

An alternative category of micro assembly is that of parallel, or guided, assembly. Guided assembly refers to the manipulation of multiple micro parts simultaneously. The benefits of this type of assembly technique are immediately apparent. The ability to assemble many micro parts in unison overcomes the speed limitation presented by serial assembly. Currently, research into parallel assembly methods centers on the use of micro-dominant forces as a driving force for the assembly process. Common micro-dominant forces utilized for micro assembly include electrokinetic, thermal, electromagnetic, and even acoustic forces. As such, these techniques provide additional advantages as compared to serial techniques as it eliminates the need to miniaturize the tool used for fabrication to obtain better resolution.

Recent, research into parallel micro assembly techniques has yielded encouraging results. For example, a 2014 study conducted by a team at Harvard Medical School successfully demonstrated the use of paramagnetism of free radicals to perform guided assembly of magnetically tunable gels for use in bottom-up tissue engineering [20]. In 2011, a paper published in the Journal of Micromechanics and Microengineering detailed the creation of microbiorobots from motile microorganisms whose movement could be controlled by ultraviolet light to facilitate two-dimensional movement of micro parts [21]. More recently, researchers at the University of California Irvine successfully assembled polystyrene beads onto patterned electrode arrays via dielectrophoresis [22].

The advantages provided by parallel micro assembly make it an obvious choice for future development of industrial scale micro assembly techniques. However, in order for this to occur, there are a number of challenges presented by parallel assembly methods that must be overcome. Firstly, the micro-dominant forces that micro parts experience are often complex and require knowledge of the system’s chemical, physical, and electrical properties, such as the case with dielectrophoresis or electroosmosis. Even when these properties are known, these forces can be extremely difficult to model or calculate as these forces often act simultaneously on multiple micro parts.. As such, different approaches to study and characterize the use of the micro-dominant forces to manipulate micro parts must be established to create viable parallel assembly processes.

The following sections of this thesis describe in detail novel research conducted on the use of parallel assembly driven by dielectrophoresis, an electrokinetic force dominant in the microdomain, to create robust micro structures capable of solving real-world challenges. Chapter Two presents a novel process to repair fractured microelectrodes through DEP driven assembly of carbon nanotube bridges [23]. This research highlights the usefulness and benefits of guided micro assembly. Building upon this, Chapter Three presents research that exploits advances in modern artificial intelligence to take a phenomenological approach to characterizing the effect of dielectrophoretic force on micro particles [24]. This research establishes an alternative method for such characterization without the need for complex modeling or calculation.

The results of both of these studies serve as a proof of concept for the development of new parallel micro assembly techniques capable of being performed at scale to solve real-world technical challenges. Miniaturization continues to be an important tool across many fields to further push the boundaries of science and technology. Additionally, challenges facing society today relating to climate change and depletion of finite natural resources, place increased importance on the ability to continue to miniaturize devices. Research into parallel micro assembly, such as that presented in this work, is of critical importance to further improve the r ability to produce micro devices quickly and economically.

Chapter 2 – Guided Healing of Microelectrodes Via Electrokinetic Assembly of Carbon Nanotube Bridges

2.1 Chapter Introduction

As modern society becomes increasingly reliant on electronic and micro devices, the durability, reliability, and lifespan of the constituent components of these systems, in particular their electrodes and similar conductive interconnections, is becoming increasingly critical. This is compounded by the rapid development of new micro and nano scale fabrication technologies that enable such components to be created at increasingly small length-scales [25-28]. The use of components at such length scale, combined with newly emerging applications for such devices, exposes them to increasing risk of failure. In particular, microelectrodes at the micro and nano scale are at an increased risk of damage stemming from thermal, chemical, and mechanical stresses [27-29]. As such, research into methods to repair microelectrodes and other micro and nano scale components is of growing importance to impart better longevity and reliability to micro devices while also reducing waste and redundancy [28-31].

A significant portion of the existing research on the subject of microelectrode repair is centered around the self-restorative polymer materials used to encapsulate microelectrodes and facilitate the self-healing of discontinuities that may form. In 2013, a hydrogen-bond directed self-healing polymer binder was present by Wang, C. et al. which was successfully used to repair fractures in silicon electrodes resulting from cyclic electrochemical processes, and subsequent cyclic volumetric changes, within lithium ion batteries [32]. Similarly, in 2018, Wang, Y. et al. presented a repairable microelectrode fabrication technique through sputtering of gold onto polymetric microfibers that enabled heat treatment as a repair mechanism. The research group demonstrated the when the conductive gold coating was fractured due to external stresses, heat treatment successfully shrunk the underlying microfiber structures, bringing the gold back into contact and restoring conductivity [34]. Further research has expanded upon these concepts, such as the 2019 paper published by Sim et al., which demonstrated that encapsulation in liquid crystal graphene oxide offered better restoration of conductivity, in addition to improve tensile strength, as compared to more traditional polymers [33].

Other research into this topic has sought to develop more flexible and durable conductive substrates and metals to reduce the likelihood of failure. Such materials have been studied extensively in the field of biomimetic films to increase the tensile strength of electrodes and other micro-electronic components [36]. Whereas some researchers have opted to replace traditional electrode materials all together. For example, a 2013 article published by Liu et al. details a direct-printed liquid-metal GaInSn alloy film for use as a conductive and highly compliant electrode within dielectric elastomer actuators. The presented film demonstrated strong flexibility as well as stable resistance across the electrode with increasing amounts of induced strain. This film was also found to be capable of two-dimensional self-healing further improving the reliability and longevity of the proposed material [35].

The approach to repair microelectrodes within this research focuses on the use of conductive Carbon Nanotube Bridges (*CNTs*) in conjunction with a guided electrokinetic assembly method to restore conductivity across fracture microelectrodes. Since their discovery in 1991 [A], CNTs have become a widely-used component and material within a variety of microelectronic devices from batteries and sensors to integrated circuits [38-39].

Existing literature outlines a variety of mechanisms by which CNTs can be manipulated, assembled, and integrated into micro-components [40-41,22]. This research centers on micro-electrokinetic assembly, which utilizes electrical forces dominant in the micro domain, to manipulate particles into micro structures. Specifically, this research employs Dielectrophoretic (DEP) force to arrange and assemble CNTs.

DEP is a force that acts on micro and nano particles when the particles are subjected to a non-uniform electric field [5,42]. The electric field induces polarization of the micro particles and the resulting dipole moment of the particles align along the electric field lines. Depending on the magnitude and frequency of the applied electric field, as well as physical characteristics of both the particles and the medium they are suspended in, the DEP force either attracts the particles to or repels them from the strongest point of the electric field [5,42]. DEP force can be described using equation 1 below:

$$F_{DEP} = \frac{\pi r^2 l}{6} \varepsilon_m Re[f_m] \nabla E_{rms}^2 \tag{1}$$

Equation 1: *DEP Force*

where *l* and *r* are the length and radius of the particle respectively; ε_m is the permittivity of the medium; E_{rms} is the root means square of the electric field; and *Re*[f_m] is the real part of the Clausius-Mossotti (CM) factor, f_m, described in Equation 2:

$$f_m = \frac{\varepsilon_n^* - \varepsilon_m^*}{(\varepsilon_n^* - \varepsilon_m^*)A_L + \varepsilon_m^*} \tag{2}$$

Equation 2: *Clausius-Mossotti Factor*

where A_L is the depolarization factor, ε_n^* and ε_m^* are the complex permittivities of particle and medium, respectively, as defined by Equation 3:

$$\varepsilon^* = \varepsilon - j\frac{\sigma}{\omega} \tag{3}$$

Equation 3: *Complex Permittivity*

In addition to using DEP-driven electrokinetic assembly, this research relies on a specific method of introducing the CNTs to the process known as “Step-wise CNT Deposition”. This method, first reported in 2020 by Zhou et al. [22], requires that small droplets of CNTs suspended in isopropyl alcohol (IPA) be introduced inside the electric field sequentially, with enough time in between droplet depositions to allow the IPA solvent to evaporate fully. The research team proposed that the IPA evaporation induced capillary forces, the result of the shrinking liquid meniscus, which served to pull individual CNTs together and form a tighter and more compact resulting structure. Zhou et al. reported that this novel fabrication method is capable of producing CNT-based structures, or “bridges”, across larger gaps than previously reported and was successful in creating a CNT bridge across a 75µm gap, the largest report to date to the best of the author’s knowledge.

Despite this team’s success in assembling large CNT bridges, further research is necessary to determine if this method is feasible for microelectrode repair. Firstly, the horseshoe geometry of the electrodes used in the study were highly controlled and designed to produce strong electric fields and thus strong DEP force, however electrodes used in microdevices are typically linear in nature. Furthermore, fracture of such electrodes results in highly irregular and unpredictable electrode surfaces, far different than the controlled interfaces used in the study.

The study presented within this paper seeks to build upon the previous research described above through the assessment of the validity and feasibility of DEP-Driven Electrokinetic assembly paired with step-wise CNT deposition as a method for guided repair of microelectrodes. A viable process by which to assemble CNT bridges that successfully restores conductivity will find application in a wide array of fields in addition to microelectronics, namely biotechnology and tissue engineering. For example, in a 2009 study, Hallstrom el al. demonstrated the use of conductive nano-wire arrays for regenerative growth of neural axons [49]. Similar conductive CNT bridges may be of use in treating neurological damage such as spinal cord injuries [49-51].

2.2 Methods and Materials

2.2.1 Fabrication of Carbon Electrodes

In order to test the linear electrode geometry, numerous sets of carbon microelectrodes with pre-manufactured gaps of 20, 30, and 40 µm were fabricated using a standard lithography process and pyrolysis. Figure 1 contains a schematic of fabricated electrodes. Each electrode measured 120 µm in width, with two 5mm long segments on either side of the electrode gap. Each segment was connected to a 2mm by 2mm contact pad that was used to connect the electrode to a function generator. Additionally, a set of electrodes without a gap was fabricated to serve as control samples.

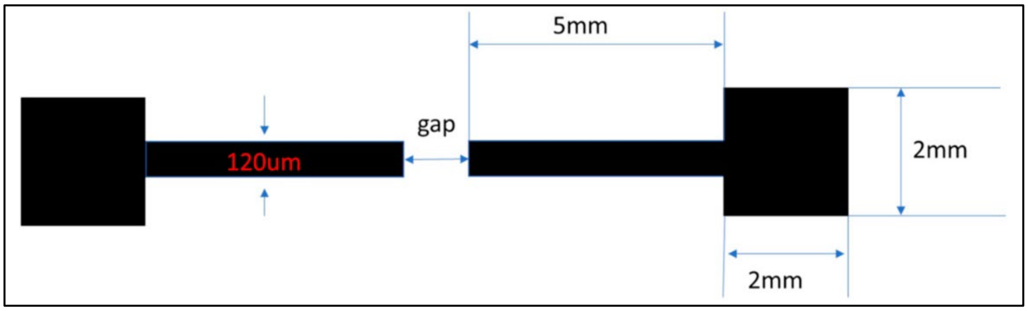

Figure 1: *Dimensional Schematic of Carbon Electrodes with Pre-Fabricated Gap*

To fabricate these electrodes, a 4 inch silicon wafer containing a 1µm silicon oxide layer (University Wafers) was spin-coated with SU-8 2015 negative photoresist (Kayaku Inc.) using a photoresist spinner (Laurell Technologies) at 500 rpm for a duration of 10 seconds followed by 4000 rpm for 30 seconds. The wafer was subsequently baked on a hot plate at 95°C for 2 minutes. Following the soft-bake, the coated wafer was exposed to ultraviolet light through a photomask (CadArt), containing the desired electrode geometry, at an energy intensity of 10mW/cm^2 for 10 seconds. The mask was aligned using a mask aligner (Karl Suss).

Following exposure, the wafer was baked again on a hot plate at 95°C for 4 minutes. The portions of photoresist not cross-linked by exposure were removed using SU-8 developer (Kayaku Inc.). The remaining photoresist pattern was baked once more at 150°C for 20 minutes.

Lastly, the remaining photoresist was converted to carbon using a pyrolysis furnace (Thermo Fisher). The pyrolysis process was initiated in a nitrogen-rich environment at 25°C for 120 minutes followed by a ramp to 300°C over 69 minutes. The wafer was held at 300°C for 60 minutes before a subsequent ramp to 900°C over 90 minutes. The wafer was held at 900°C for one hour before allowing it to cool to room temperature naturally.

2.2.2 Preparation of Carbon Nanotube Suspension

The CNT-IPA suspension was prepared by mixing 5 µg of multi-wall CNT powder (Sigma-Aldrich) into 15 mL of IPA. The solution was then centrifuged (Eppendorf AG) at 3000 rpm for 4 minutes to precipitate large agglomerations of the CNTs. The supernatant containing suspended CNTs was transferred to a clean container for use.

2.2.3 Experimental Setup

Once fabricated, initial conductivity tests were performed on the electrodes, using a multimeter, to confirm the open circuit. Then, the electrodes were connected to a function generator (Standford Research Systems) by soldering 34-gauge buss wire to each contact pad using Indium solder. The chip containing the electrode was then placed under an optical microscope (Nixon Eclipse) to observe the formation of the CNT bridges. A cMOS camera (Spot Imaging) was used to extract images from the microscope. To induce positive DEP, which would attract the CNTs to the edge of each electrode segment, the function generator was set to apply a constant AC bias at a peak-to-peak voltage of 4V and a frequency of 100kHz. The experimental setup is illustrated in figure 2.

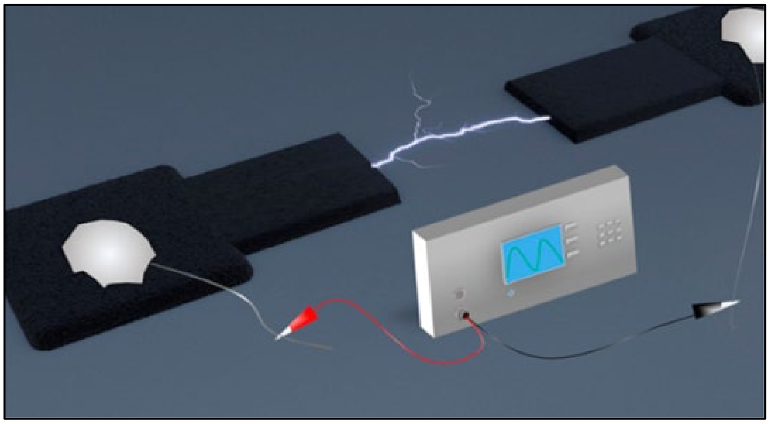

Figure 2: *Illustration of Experimental Electrode Setup*

Individual 0.5 µL droplets of the CNT suspension were pipetted into the electrode gap. Following the stepwise CNT deposition method, each droplet was allowed to fully evaporate prior to the next droplet deposition. This process was repeated until the CNT bridge spanned the length of the electrode gap, confirmed visually using the microscope.

Once the CNT bridge was assembled, the buss wire leads were disconnected from the function generator and a resistance measurement was taken across the electrode. The electrodes were probed with a multimeter at each contact pad to obtain this measurement.

2.2.4 Creation of Fractured Electrode

To replicate a microelectrode that had sustained real-world damage, a control electrode with no pre-fabricated gap was used. First the initial resistance across the electrode was measured to compare with the final resistance once repaired with a CNT bridge. Next, the electrode was fractured using a razor blade, creating a gap within the electrode with an irregular edge geometry. The resulting electrode gap was measured using an optical microscope and a lack of conductivity was confirmed with a multimeter. A CNT bridge was built across the fractured electrode following the same experimental setup and methodology detailed in section 2.2.3.

2.2.5 Preparation and Deposition of Pyrrole Suspension

Once the CNT bridges were assembled across the electrode gaps, polypyrrole (PPy) was deposited atop the samples to characterize the effects of this polymetric coating on the electrical performance and durability of these bridges.

The pyrrole solution was prepared by adding 0.1M of pyrrole monomers (Sigma-Aldrich) and 0.1M sodium dodecylbenzenesulfonate (Sigma-Aldrich) to 100 mL of deionized water. The solution was stirred continuously for 20 minutes.

To deposit the PPy coating onto the CNT bridge, the electrode was again connected to the function generator as detailed in section 2.2.3. The function generator was set to pass a DC current through the electrode at a voltage of 0.9V. Next, a 0.5 µL droplet of the pyrrole solution was pipetted on top of the CNT bridge. Due to the applied DC current, the pyrrole polymerized into PPy from one end of the bridge to the other in the same direction as the current. Two different methods of PPy deposition were evaluated. In the first method, the DC current was applied in one direction for the entirety of the deposition while in the second, the direction of the current was reversed halfway through.

2.2.6 Stress-Testing of CNT Bridges

Once assembled, the CNT bridges with and without PPy coating were tested to determine their durability when subject to various environmental stressors that typical microelectrodes may experience while in use. These stressors included forceful blasts of gas, flowing liquid and thermal cycling.

The first group of samples were subjected to a blast of nitrogen gas compressed to 88 PSI for 30 seconds. The gas flow was oriented perpendicular to the bridge. Other samples were subjected to a 0.06 LPM volumetric flow of deionized water for 30 seconds. Lastly, a third group were subjected to 10 rounds of thermal cycling. Each cycle consisted of bringing the temperature of the electrode from 3°C to 200°C using a hot plate and ice pack. The samples were allowed no residence time at either extreme of the thermal cycling process.

Before and after each test, the resistance across the healed electrode was measured with a multimeter to quantify the effect of the stressors on the efficacy with which the bridges conducted electricity.

2.2.7 Finite Element Analysis of Electric Field Magnitude

To support the experimental results obtained from the methods described in the previous sections, COMSOL Multiphysics (v. 5.2) simulation was conducted to model the strength of the electric field resulting from the application of AC bias across electrode gaps of various lengths. From this, the change in field strength that occurs as a result of the electrode gap decreasing in length as the CNT bridge forms across it could be described.

For the simulation, a triangular mess with greater than 18,000 elements was utilized. The simulation used a glassy carbon material to model the electrode with a permittivity of 108 ε_o and IPA for the medium with a permittivity of 18.23 ε_o. Boundary conditions were set to 0V on one end of the electrode gap and 4V on the other to mimic the experimental setup. A standard COMSOL linear solver was used to solve the governing system of equations.

2.3 Results and Discussion

2.3.1 CNT Bridge Assembly Across Pre-Fabricated 20, 30, and 40 µm Gaps

Using the procedures detailed in Section 2.2, CNT bridges were successfully assembled across all pre-fabricated electrode gaps ranging from 20 µm to 40 µm in length. CNT bridges were assembled across 3 samples each of the 20, 30, and 40 µm gaps. Images in Figure 3 through Figure 5 are from the cMOS camera connected to the microscope taken throughout the CNT bridge assembly process, depicting the sequential formation of the CNT bridges. It can be seen in these images that, as expected, the CNTs were attracted to the edges of each electrode segment due to the induced positive DEP force. These images also show that the total amount of CNT suspension required to form the bridges increased with electrode gap length.

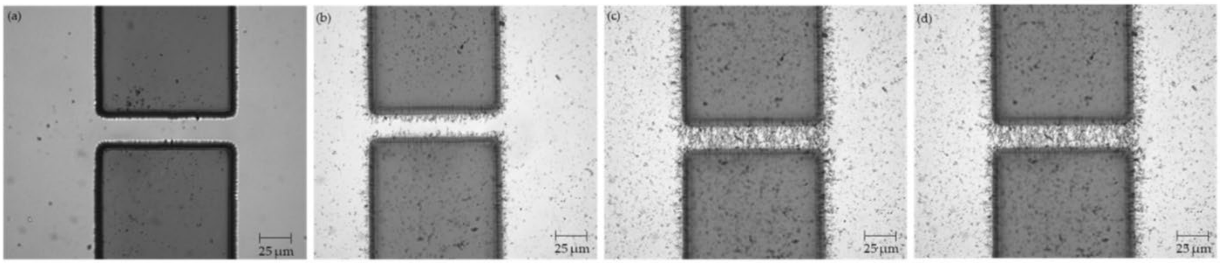

Figure 3: *Electrodes with 20 µm gap (a) before CNT deposition; (b) after 2 µL of CNT suspension; (c) after 4 µL of CNT suspension; (d) after 5 µL of CNT suspension.*

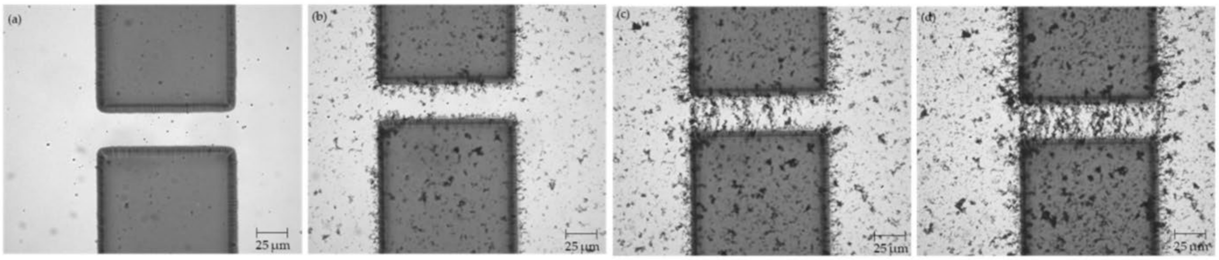

Figure 4: *Electrodes with 30 µm gap (a) before CNT deposition; (b) after 3 µL of CNT suspension; (c) after 7 µL of CNT suspension; (d) after 10 µL of CNT suspension.*

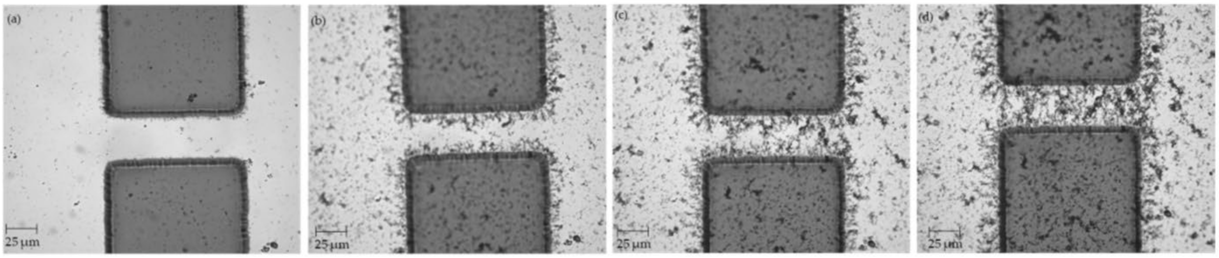

Figure 5: *Electrodes with 40 µm gap (a) before CNT deposition; (b) after 5 µL of CNT suspension; (c) after 7 µL of CNT suspension; (d) after 10 µL of CNT suspension.*

2.3.2 Resistance of CNT Bridges and Conductivity Restoration

The resistance of each sample was measured following the completion of CNT bridge assembly. The average final resistance of the three samples for each electrode gap size, as well as the resistance measurement of the control sample, are reported in Table 1 below.

***Table 1:** Average resistance measurements of healed 20, 30, and 40 µm electrodes.*

ELECTRODE GAP LENGTH (µM)	AVG. RESISTANCE MEASUREMENT (STD. DEV.)(KΩ)
ELECTRODE PRIOR TO FRACTURE (CONTROL)	5.80 (± 0.61)
20	15.61 (± 1.85)
30	19.11 (± 1.88)
40	31.88 (± 6.98)

These results demonstrate that assembling CNT structures across gaps within an electrode can successfully restore its conductivity, i.e. healing it, and that electrokinetic assembly via DEP force is a sufficient technique for doing so. However, a significant increase in resistance is observed when comparing the healed electrodes to the control sample. The healed samples had an average increase in resistance of 169%, 229% and 449% for the 20, 30, and 40 µm CNT bridges respectively. Thus, the restored conductivity across the electrode came at the price of significantly higher resistance.

Figure 6 provides a graphical representation of these results in which the average resistance is plotted as a function of CNT bridge length. The data demonstrates that the final resistance across the healed electrode increases with the length of the CNT bridge and that this relationship is non-linear. Previous research determined that resistance within CNT structures arises not across individual tubes, but rather across the CNT-to-CNT contact junctions [52-53]. The findings presented here support this conclusion. The non-linear relationship between resistance and CNT bridge length is likely the result of an exponentially increasing number of CNT-to-CNT junctions as the bridge length is increased.

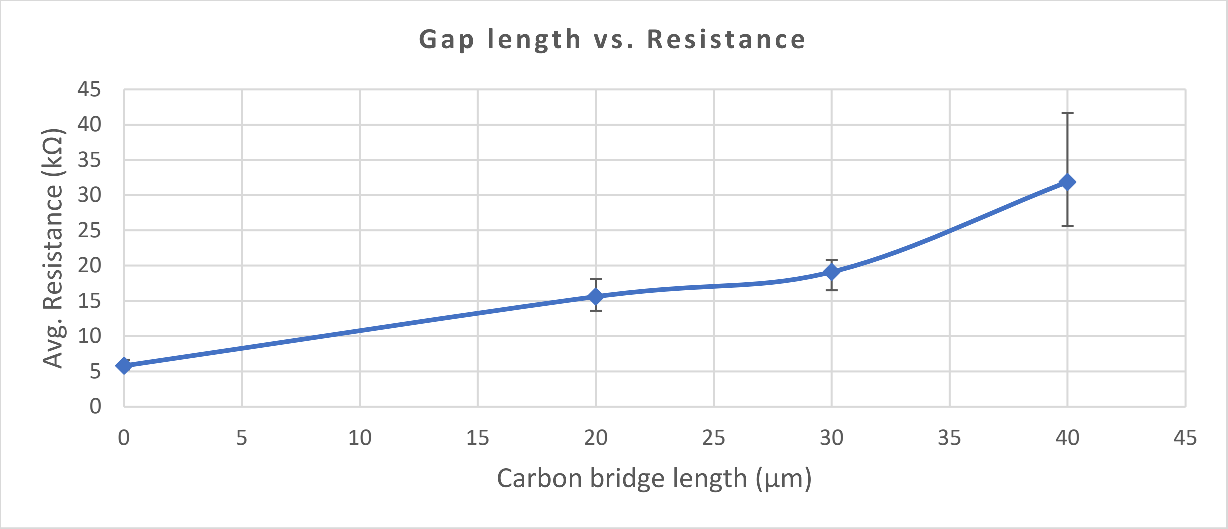

Figure 6: *Plot of the average resistance across the healed electrodes as a function of CNT bridge length.*

During assembly of the CNT bridge across one of the 30µm gap samples, the resistance across the electrode was measured after every-other 0.5 µL deposition of CNT suspension to better understand the dynamics of this conductivity restoration. These results are contained in Table 2 below.

Table 2: *Resistance measured across an electrode with 30 µm gap after every other 0.5 µL droplet of CNT suspension.*

TOTAL AMOUNT OF CNT SUSPENSION (µL)	RESISTANCE (KΩ)
1	Open Circuit
2	Open Circuit
3	Open Circuit
4	Open Circuit
5	Open Circuit
6	Open Circuit

7	Open Circuit
8	360
9	147
10	28.7

As anticipated, once conductivity was restored, the resistance across the electrode decreased exponentially with each subsequent droplet of CNT suspension. To further understand this finding and the morphology of the CNT bridge, highly magnified images of this sample were taken using scanning electronic microscopy (see Figure 7). As seen in the images, the CNT bridge is, in reality, a collection of micro bridges that form individual pathways for conduction. Based on this, it is likely that the decrease in resistance with subsequent deposition of CNT suspension is due to the assembly of additional complete pathways capable of conducting electricity across the bridge.

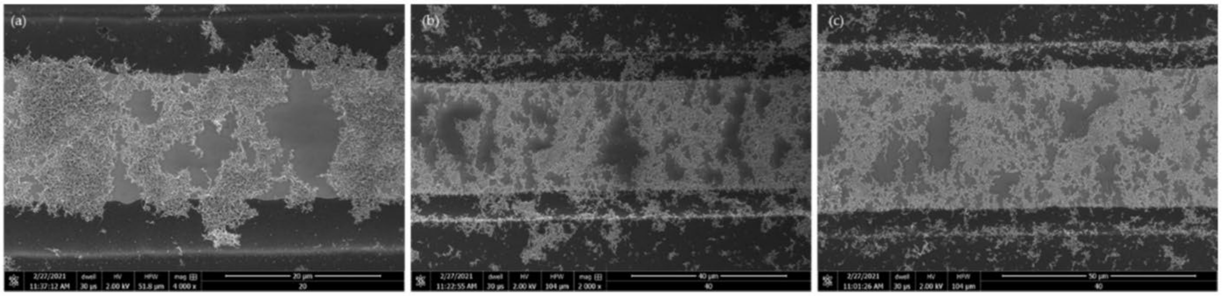

Figure 7: *Scanning electron microscope (SEM) pictures of the CNT bridges formed across (a) 20 µm electrode gap (b) 30 µm electrode gap (c) 40 µm electrode gap.*

2.3.3 Finite Element Electric Field Simulation

In order to understand the relationship between the electric field strength and the length of the electric gap, a COMSOL Multiphysics simulation was conducted following the procedure outlined in section 2.2.7. The results of this simulation are presented in Figure 8 below. The outcomes indicate that, as anticipated, based on Coulomb's law of the magnitude of electric fields [54], the strength of the electric field is inversely proportional to the distance over which it spans.

As the CNT bridges begin to form from each side of the electrode gap, the effective length of the gap becomes increasingly smaller, leading to the strength of the induced electric field across the gap to become increasingly stronger. Given that the magnitude of the DEP force responsible for attracting CNTs to form the bridge is proportional to the strength of the electric field, it is evident that the proposed electrokinetic assembly method is self-reinforcing. That is, as the process proceeds, the driving DEP force becomes stronger and additional CNTs are more readily attracted to the forming bridge. This result is of critical importance to understanding the physics behind this assembly technique and assessing its ability to form conductive bridges across larger electrode gaps than previously thought feasible. The increase in resistance across the forming CNT bridge as it becomes longer is offset by the simultaneous increase in electric field strength and, subsequently, the DEP force, due to the decreasing gap length allowing continued assembly of the bridge.

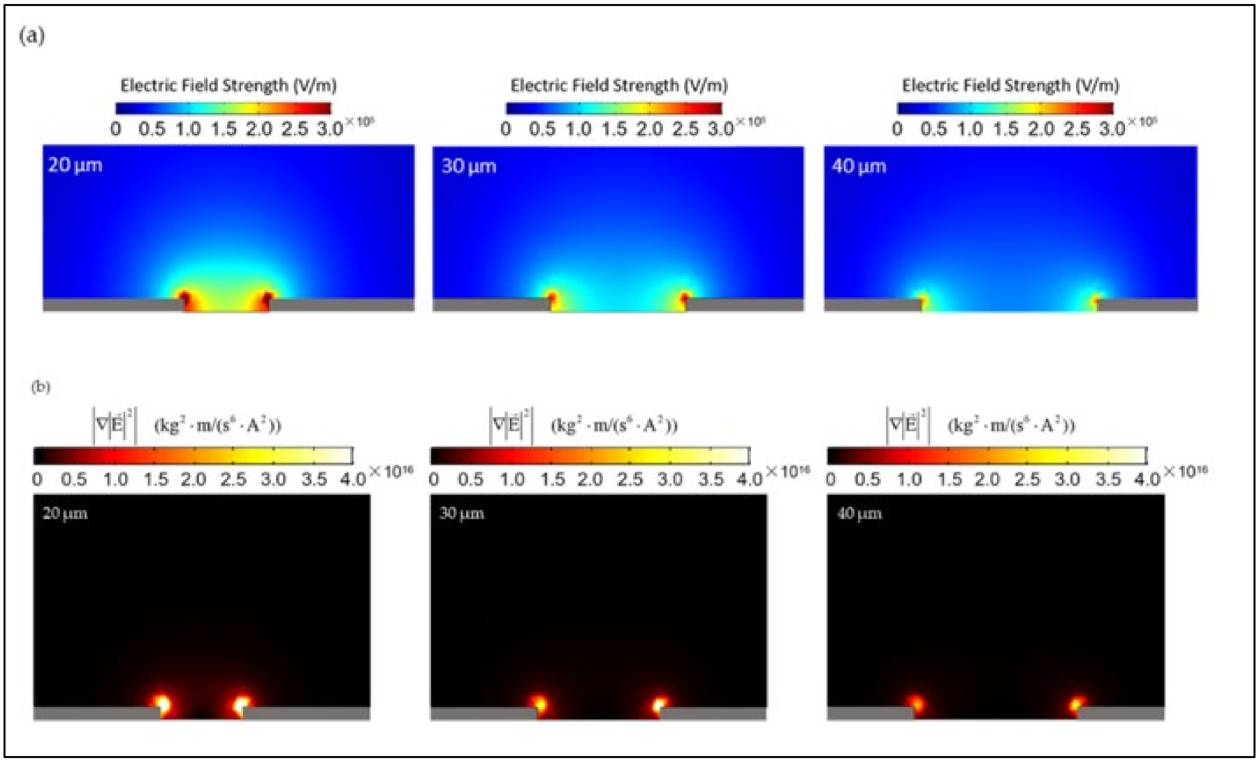

Figure 8: *Simulation across electrode gap lengths of (a) the electric field strength (b) the gradient of the square of the electric field strength.*

2.3.4 CNT Bridge Assembly over Fractured Electrode

As detailed in Section 2.2.4, a fractured electrode, mimicking a real-world damaged microelectrode, was created by mechanically fracturing an intact electrode with a razor blade. The resulting electrode gap consisted of irregular edge geometries as shown in Figure 9. The gaps were measured at their shortest section at approximately 170 µm and 310 µm at the widest point. Multimeter analysis confirmed the electrode was no longer capable of conducting electricity.

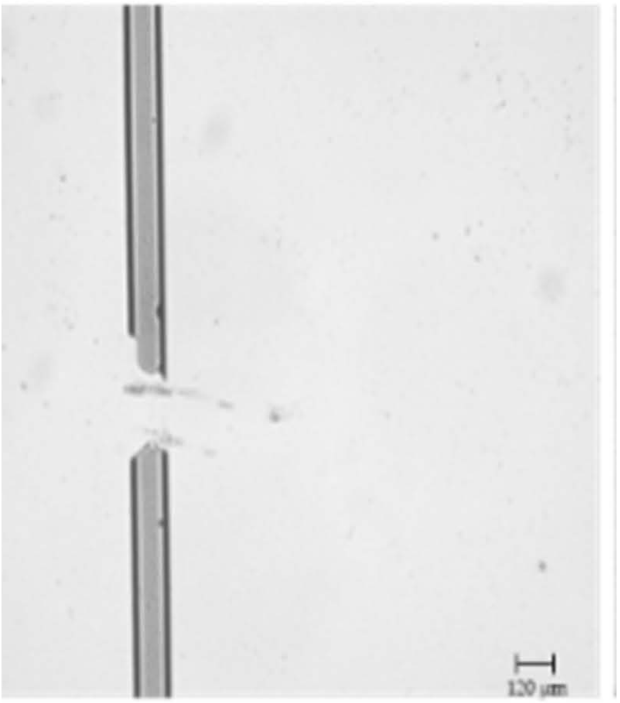

Figure 9: *Image of fractured electrode with irregular edge geometry.*

Using the same experimental setup and processes detailed in Section 2.2, a CNT bridge was successfully formed across this gap - a total of 23 µL of CNT suspension. The resistance of the healed electrode was found to be 239.6 kΩ, a 4031% increase compared to the resistance of the electrode prior to fracture. Despite this significant increase in resistance, this result serves as proof of concept that the proposed electrokinetic assembly technique is capable of forming CNT bridges across larger gaps than previously reported (150 µm). Furthermore, this result confirms that the irregular edge geometry of each electrode segment did not prohibit the assembly of the CNT bridge using this technique, an important finding that supports the use of such methods for repair of microelectrodes under real-world conditions. Images taken during various stages of the assembly process are included in Figure 10.

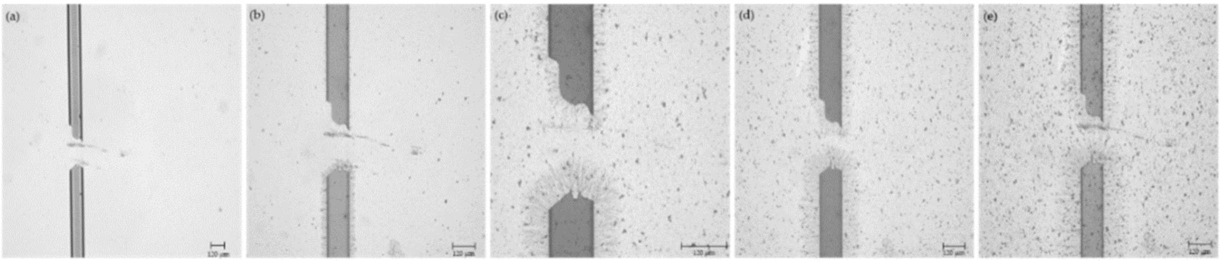

Figure 10: *Fractured electrode (a) before CNT deposition; (b) after deposition of 7 µL of CNT suspension; (c) after 15.5 µL of CNT suspension; (d) after 19 µL of CNT suspension; and (e) after 23 µL of CNT suspension.*

2.3.5 Deposition of Polypyrrole

Under an applied 0.9V DC bias, the CNT bridges were successfully coated in a layer of PPy. Both methods for deposition, one in which the direction of the current was held constant and the second in which it was reversed halfway through deposition, were found to be effective in depositing this coating. The only observed difference between these two methods was the lateral width of the resulting PPy layer. When the polarity of the bias was held constant, the lateral width of the PPy layer was larger compared to when the polarity was inverted halfway through deposition. Images taken during the PPy deposition process are presented in Figure 11 and Figure 12 below.

It should be noted that the resulting resistance of the electrodes after PPy was deposited was significantly less than the uncoated samples. This is can be attributed to the to the fact that PPy is a conductive polymer that aids in the conduction of electricity across the CNT bridge. The average resistance across 30µm CNT bridges coated with PPy was found to be 1.2 (standard deviation ±0.20), representing a 93% average decrease in resistance compared to the uncoated sample. As such, use of the CNT bridges as a substrate for deposition of PPy is an effective way to heal the electrode with better conductivity performance.

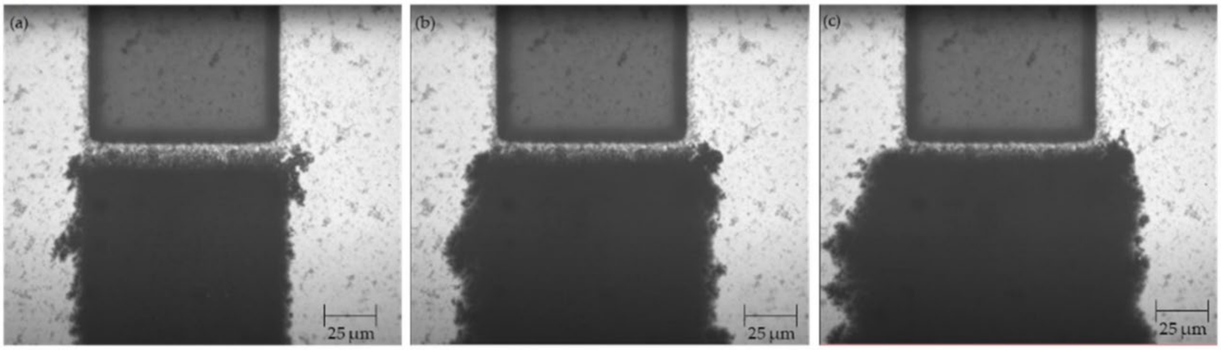

Figure 11: *Results of polymer polypyrrole (PPy) deposition over the CNT bridge spanning 20 µm electrode gap without switching the polarity of 0.9 Vpp DC bias captured at approximately (a) 25%completion (b) 50% completion (c) 100% completion.*

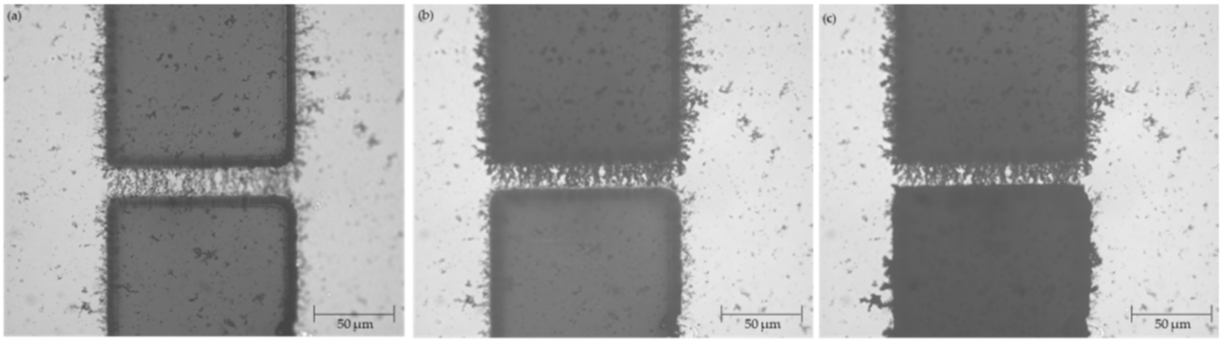

Figure 12: *Results of PPy deposition over the CNT bridge spanning 20 µm electrode gap (a) prior to PPy application; (b) after the PPy deposition from the side of the top electrode reached roughly half-way through the CNT bridge and the polarity of the 0.9 Vpp DC.*

2.3.6 CNT Bridge Stress-Testing

Per the process outlined in Section 2.2.6, samples of healed electrodes with 30 µm CNT bridges were stress-tested. Based on the results contained in Table 3, no significant change to the resistance of the CNT bridge samples was observed as a result of blasting the samples with compressed Nitrogen. There was also no significant difference found after subjecting samples to flowing deionized water, as shown by the results in Table 4. Both results indicate that the CNT bridges are fairly durable and able to withstand moderate mechanical stressors.

Table 3: *Resistance measurements before and after blasts of compressed nitrogen gas over healed electrode samples.*

SAMPLE	RESISTANCE PRIOR TO BLAST OF COMPRESSED NITROGEN (KΩ)	RESISTANCE AFTER BLAST OF COMPRESSED NITROGEN (KΩ)
WITHOUT PPY COATING	23.4	23.0
WITH PPY COATING	1.26	1.24

Table 4: *Resistance measurements before and after flow of deionized water over healed electrode samples.*

SAMPLE	RESISTANCE PRIOR TO FLOW OF DI WATER (KΩ)	RESISTANCE AFTER FLOW OF DI WATER (KΩ)
WITHOUT PPY COATING	23.0	24.8
WITH PPY COATING	1.41	1.50

However, when samples were subjected to thermal cycling, a significant change in resistance was observed for both coated and uncoated samples. As shown in Table 5, the sample without the PPy coating experienced a 19% decrease in resistance due to thermal cycling, while the coated sample's resistance increased by 17%. This is thought to be due to additional evaporation that occurs during the heating involved in the thermal cycling process. The additional evaporation through surface tension forces of the shrinking meniscus further pulls individual CNTs tighter together, reducing the resistance across the CNT-to-CNT junctions. On the coated sample, however, the PPy is thought to have prevented this additional evaporation from occurring.

Table 5: *Resistance measurements before and after Thermal Cycling of healed electrode samples.*

SAMPLE	RESISTANCE PRIOR TO THERMAL CYCLING (KΩ)	RESISTANCE AFTER FLOW OF DI WATER (KΩ)
WITHOUT PPY COATING	23.0	24.8
WITH PPY COATING	1.41	1.50

2.4 Chapter Summary

The presented study serves as a proof of concept that guided electrokinetic assembly via DEP force to form conductive CNT structures is a viable method to repair damaged microelectrodes. Combination of this assembly technique, alongside utilization of a stepwise CNT deposition technique, was successful in creating CNT bridges across larger electrode gaps than previously reported, including formation across gaps with irregular edge geometries, a key feature of real-world fractures within microelectrodes. The non-linear relationship developed between resistance and the length of the CNT bridge confirms previously reported conclusions that the largest contribution of resistance across CNT structures is the CNT-to-CNT contact junctions. Furthermore, the results of this study indicate that the use of such CNT bridges as a substrate for conductive polymetric coating can successfully reduce the resistance across the repaired electrodes.

The results of the COMSOL simulation included in this study illustrate the benefits of using an electrokinetic parallel assembly method. In addition to assembling many CNTs simultaneously, the process was demonstrated to be self-reinforcing, as the DEP force driving the assembly increased as the process proceeded. This is an example of the exploitation of the forces dominant in the micro domain to drive the formation of micro structures with more efficiency and effectivity than could be achieved using serial or top-down assembly methods.

While further study of the presented electrokinetic assembly process is required to fully understand its physics and develop a commercially viable method by which to carry out this process, the capabilities demonstrated within this research represent an exciting prospect for its use across a variety of applications and technological fields. For example, recent developments in microencapsulation technologies [55-59] could be used to encapsulate CNT suspension alongside microelectrodes within electric micro systems. Self-testing devices could then utilize the CNT suspension and the application of

AC bias across identified damaged electrodes or conductive traces to self-repair the fracture. Additionally, the use of electrokinetically assembled CNT structures to repair damage within neurological networks, such as within the human nervous system, is an intriguing example of a potential application of this technology within the medical and biotechnology fields.

Chapter 3 – Artificial Intelligence Algorithms Enable Automated Characterization of the Positive and Negative Dielectrophoretic Ranges of Applied Frequency

3.1 Chapter Introduction

Over the last few decades miniaturization has served as the cornerstone of progress in a wide breadth of fields including computing, biotechnology, material science, and communications [60-63]. Miniaturizing devices to the micro and nano scales carries a number of benefits including increased operational speed, cheaper costs and lower operational energy demand, the ability without increasing the device footprint, and a reduction in the amount of required material as well as material waste [5]. A simple example of these benefits is smartphone technology, which through miniaturization has enabled massive computational power to be packed into a pocket-sized device.

However, as miniaturization efforts proceed and manufacture of increasingly smaller micro and nano component is required, the speed and precision of available micro-assembly technologies is often a gating issue [64]. The goal of modern micro-assembly technologies is to position, orient, and assemble microscale components into complex micro structures and components through processes which have high yield and competitive costs [65]. Many such technologies are available today and many more are actively being researched and development. These technologies generally fall into one of two categories: serial or parallel assembly.

Serial assembly, commonly referred to as pick-and-place assembly, is the process of selecting, moving, and placing individual micro parts into designated locations. Microgrippers are a common tool used for serial assembly [66-68]. More advanced technology has been developed in recent years to include non-contact methods of picking parts such as through capillary force [69] or fluidic forces resulting from vibration of piezo actuators [70]. Additionally, integration of robotics into serial assembly methods has been studied in an attempt to make the process faster [71].

Despite these efforts, while serial assembly is effective and suitable when only a few micro parts require assembly, such techniques are too slow. The low throughput of these methods make them unfeasible for many micro-assembly applications on a commercial scale. Additionally, in order to improve the resolution of these technologies, increasingly smaller tools must be developed and implemented. This is a costly and unsustainable proposition.

In contrast to serial assembly, parallel micro-assembly techniques offer a number of advantages. The term parallel assembly may refer to either self-assembly, in which parts autonomously assembly into structures in response to a controlled environmental condition, or directed assembly in which multiple micro parts can be manipulated and assembled simultaneously.

Research into micro-origami in which micro parts fold into 3D structures in response to magnetic fields is a recent example of development of self-assembly techniques [74-75]. Directed assembly techniques often exploit forces which are dominant in the micro domain, most common among these are charge-based forces known as electrokinetic forces [42]. Once such force which has become of increasing interest in the field of directed micro-assembly is Dielectrophoresis (DEP). DEP force acts on polarizable dielectric particles when they are subjected to a non-uniform electric field. DEP force can either attract the particles toward, or repel them away from, the location of highest magnitude within the electric field based. Attraction is known as positive DEP force (pDEP) and repulsion is known as negative DEP force (nDEP). The governing equation for DEP force acting on a spherical particle, first introduced in chapter 2 as Equation 1 is provided again below. The sign of the DEP force is dependent on the sign of the real portion of the Claussius-Mossotti factor, f_m , introduced by chapter 2 as equation 2 and provided again below, where ε^* stands for the complex permittivity with the p and m subscripts identify the particle and suspension media respectively.

$$F_{DEP} = \frac{\pi r^2 l}{6} \varepsilon_m Re[f_m] \nabla E_{rms}^2 \tag{4}$$

Equation 4: *DEP Force*

$$f_m = \frac{\varepsilon_n^* - \varepsilon_m^*}{(\varepsilon_n^* - \varepsilon_m^*)A_L + \varepsilon_m^*} \tag{5}$$

Equation 5*:Clausius-Mossotti Factor*

Given that the real portion of the Claussius-Mossotti factor is a function of frequency, it is possible to induce either positive or negative DEP force through tuning the frequency of the applied AC bias. As such, through adjustment to frequency, the particles can be manipulated to attract to, or repel from the strongest point of the electric field, often the edge of the electrodes used to create the AC bias. It also follows that there exists a certain frequency at which the DEP force is zero. This is known as the crossover frequency, and it differs based on the characteristics of both the particles and medium [76]. Figure 13 below illustrates an example of the real portion of the Claussius-Mossotti factor as a function of the frequency of applied AC bias for spherical particle. The figure demonstrates that as the frequency approaches the crossover frequency value, the DEP force decreases in magnitude. The crossover frequency is an important process parameter when attempting to use DEP force to manipulate micro parts.

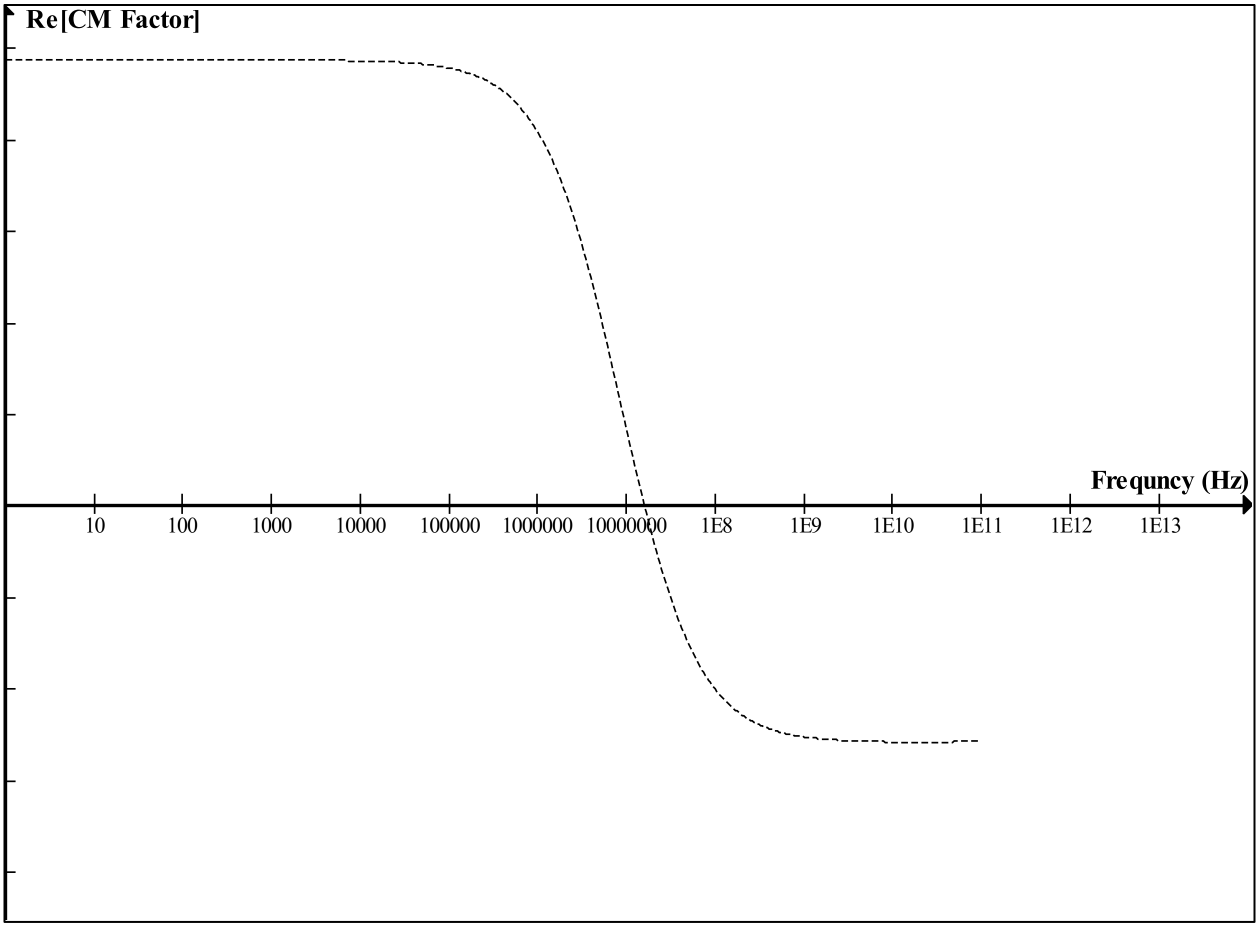

Figure 13: *The Real portion of the Claussius-Mossotti Factor as a function of Frequency for spherical polystyrene beads.*

Due to the fact that DEP force is also dependent on the shape and size of the particle it is acting on, DEP force has been widely used as a mechanism of sorting and segregating heterogenous mixtures of micro particles, including living cells and viruses [77-78]. For example, in 2020 Han et al. published research detailing the use of DEP force to separate mixtures of Salmonella and macrophages in order to perform microfluidic cellular assays with better precision [79]. Other DEP driven separation research has focused on its use for oncology diagnostics [80]. A 2014 study successfully demonstrated the use of DEP to separate circulating cancer cells from blood samples [81]. The researchers conclude the use of DEP provided a number of advantages to traditional methods including that it was dependent on the surface markers of the cancerous cells and that it was less destructive, leading to higher volumes of viable samples for test. DEP force is a clear example of the benefit electrokinetic driven parallel micro-assembly can provide over more established serial assembly methods. The speed and throughput advantages of parallel assembly is critical to the development of full-scale commercially viable micro-assembly processes.

However, parallel assembly which relies on electrokinetic driving forces presents a major challenge in that these forces must be calculated and modelled in order to predict the response they will elicit from micro particles. DEP force for example is governed by a complex set of equations that include physical and electrical properties of the particles, such as their complex primitivities and conductivities, which are difficult to ascertain, and often must be back-calculated from indirect observation of the DEP crossover frequency [84]. estimated through tightly controlled experiments. Further complications arise due to the fact that is it often difficult or impossible to isolate individual electrokinetic forces, as multiple forces are acting on and contributing significantly to the particle movement. Unlike the macro domain in which only a few forces are dominant, particles in the macro domain can experience many dominant forces contributing significantly to their movement [42]. Thus, the modelling requirements for even simple system becomes exponentially more challenging as all forces present must be accounted for. Given the number for active forces and their complexity, modelling and prediction of particle movement in response to environmental stimulus is extremely challenging and a limit factor for widescale adoption of electrokinetically driven micro and nano assembly.

The study presented in this chapter proposes an alternative method for the determination of DEP crossover frequency through an artificial intelligence (AI) driven phenomenological approach. The system described in this research was designed to determine ranges of applied AC bias frequency for pDEP, nDEP and the Crossover Frequency of a system containing 3 µm polystyrene beads suspended in deionized (DI) water. In order to calculate this information from the governing equations of DEP force, the electrical conductivity and permittivity of the DI water and polystyrene beads would be required. While the permittivity for these materials can be found in existing literature [83], the previously described issue arises as the electrical conductivity of the microbeads is not measured directly. Rather, it is deduced indirectly through experimental observation of the crossover frequency and back calculation[84]. Therefore, a phenomenological approach to finding crossover frequency is preferrable as calculation or modelling cannot be performed without experimental observation to begin with.

The automated AI-based system presented in this study is a novel approach to DEP frequency range estimation. It relies on a cyber-physical and closed-loop feedback system. The system used a function generator to apply AC bias across an electrode setup. The function generator was connected to a computer and was controlled using a custom-built AI. Using a cMOS camera attached to a microscope, the program was capable observing and automatically analyzing the movement of 3 µm polystyrene beads in response to the AC signal. Based on that analysis, the program used algorithmic AI to change the frequency of the signal and repeat the analysis. The result of this closed-loop analysis are frequency ranges in which the beads experience pDEP force (attraction to the electrodes), nDEP force (repulsion from the electrodes), and ranges in which DEP force is too weak to move the beads, i.e. the crossover frequency range.

The phenomenological approach to electrokinetic driven guided micro-assembly presented in this research represents a novel technique by which DEP force regimes at given frequencies of applied AC bias can be estimated while circumventing the challenge of complex modelling or calculation. This technique is likely to prove useful in a variety of applications in fields such as electronics, biotechnology, and tissue engineering.

3.2 Materials and Methodology

3.2.1 Fabrication of Interdigitated Electrodes

Gold interdigitated electrode arrays (IDEAs) were used to generate a non-uniform electric field for experimentation in this study. These electrodes were fabricated though a standard lithographic process paired with electron beam evaporation. Positive photoresist (Shipley) was spin-coated onto a 4 inch silicon wafer (University Wafer). The spin coater (Laurell) was set to 3000 rpm for 30 seconds, followed by 500 rpm for 10 seconds. After coating, the wafer was baked on a hot plate at 90°C or 30 minutes. Following baking, the coated wafer was exposed to UV light at an intensity of 10 mW/cm^2 for 4 seconds through a photomask (CADArt) containing the electrode pattern. The mask was aligned using an MA56 mask aligner (Karl Suss). The exposed portion of photoresist was removed with DI water.

A gold layer was then deposited onto the wafer through electron beam evaporation in a CV-8 evaporation (Airco). First a 300 Å layer of Chromium was deposited followed by a 300 Å layer of Gold. All remaining photoresist was then removed with acetone. The result of these processes was a finished wafer patterned with metal interdigitated electrodes. Each electrode consisted of 12 individual fingers spaced 70 µm apart. An image of this electrode geometry is provided in Figure 14.

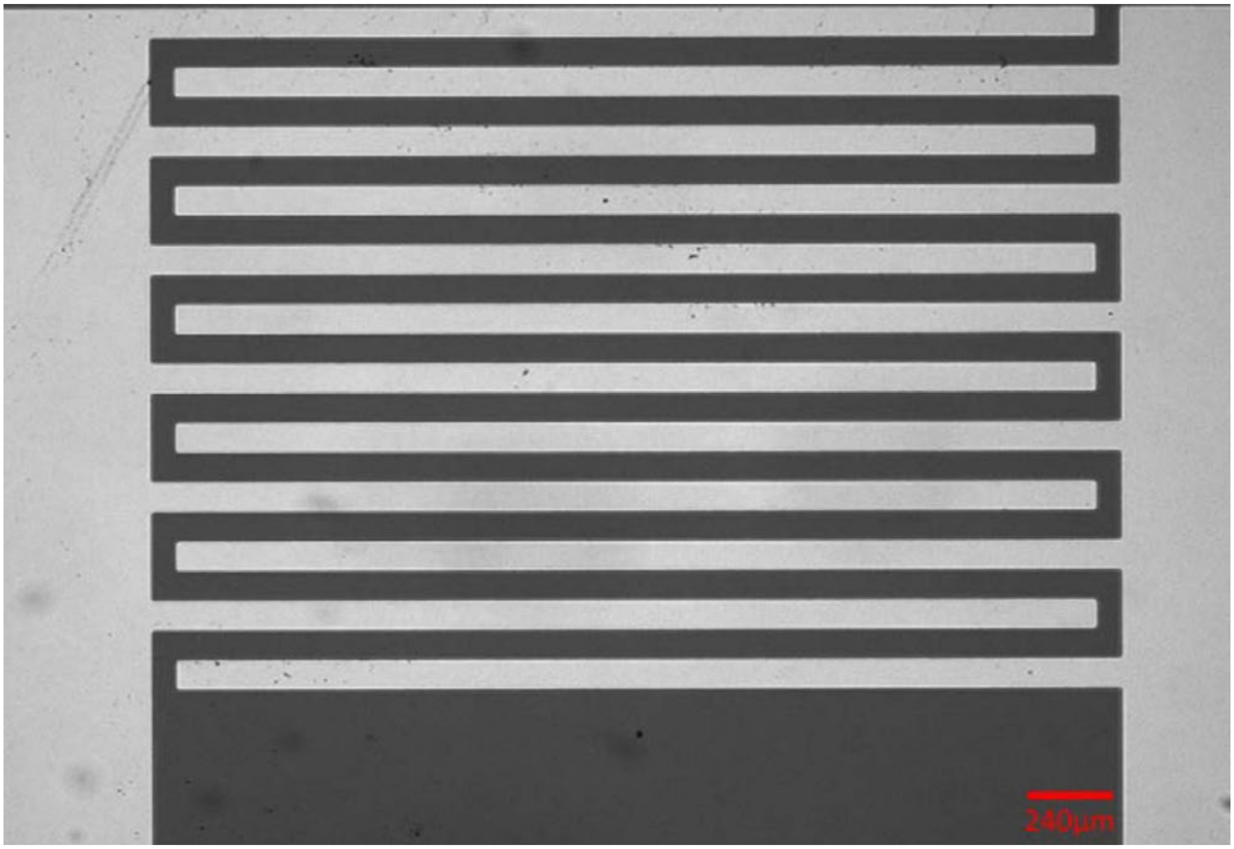

Figure 14: *The schematic of the IEDA. The gold electrode fingers (light against the dark background of the substrate) have the spacing between the adjacent fingers of 70 µm.*

3.2.2 Preparation of Polystyrene Bead Suspension

To prepare the suspension, an 4 wt% aqueous solution of 3 µm carboxyl modified latex polystyrene beads (Thermo Fisher Scientific) was diluted with DI water to a concentration of 0.39 wt%. The suspension was centrifuged (Eppendorf) at 2000 rpm for 20 minutes to remove large agglomerations of beads. The supernatant was pipetted out of the mixture and placed in a clean container for use.

3.2.3 Experimental Setup

To conduct the experiment, the electrode was connected to the function generator using 34 gauge buss wire soldered to the electrode contact pads with indium. Adhesive tape was used to construct a cage to confine the bead suspension to the location of IDEA as shown in Figure 15. The function generator (Stanford Research Systems) was connected to a PC which used the Standard Commands for Programmable Instruments (SCPI) programming language in conjunction with the Virtual Instrument Software Architecture (VISA) to control the settings of the generated AC bias, including Peak-to-Peak voltage (Vpp) and frequency.

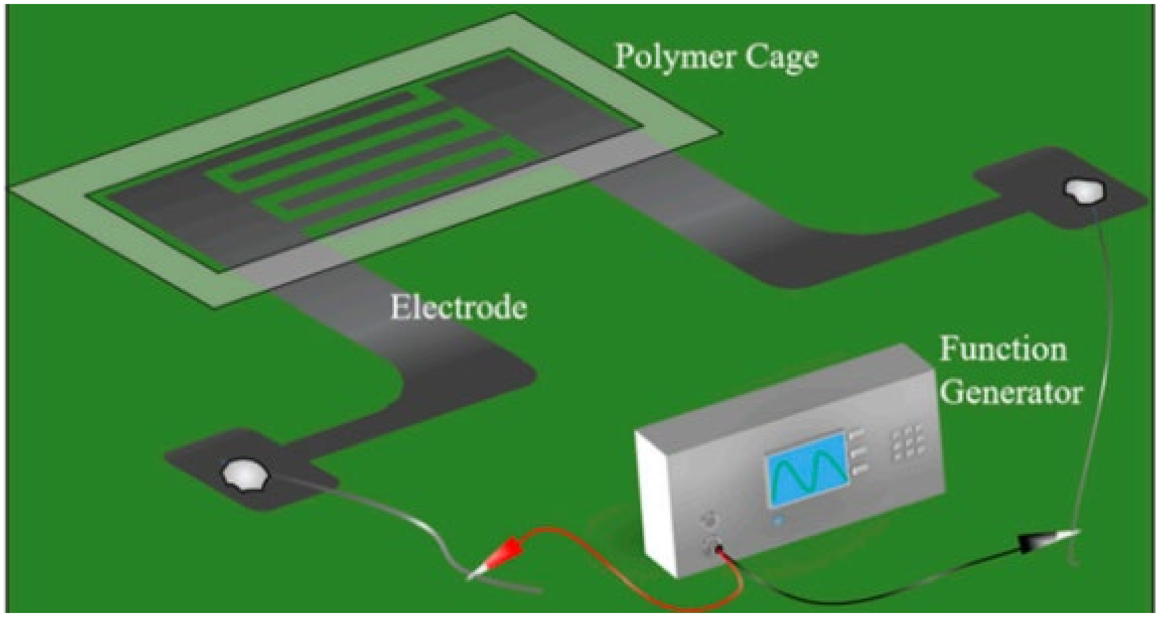

Figure 15: *Visual representation of the physical IDEA experimental setup.*

A 10 µL droplet of bead suspension was deposited onto the IDEA. The function generator was programmed to apply an AC bias at 3 Vpp. The AI software then changed the frequency of the applied bias to study the bead response. The entire setup was placed under an optical microscope (Nikon) containing a cMOS camera (Spot Imaging) in order for the AI software to observe and record bead movement during the experiment.

3.2.4 Software Architecture Overview

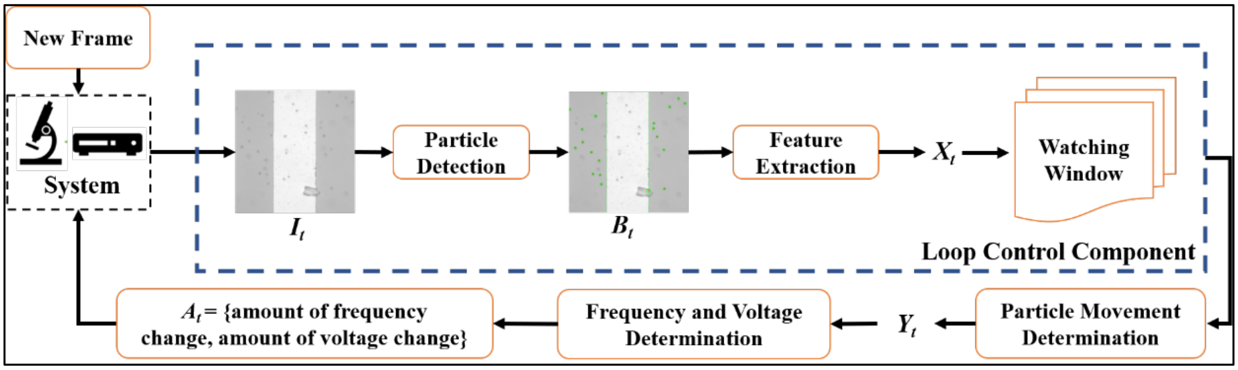

Figure 16: *Visual representation of the AI software program architecture.*

Built with the Python programming language, the custom-built software used in this study was designed to observe and recognize the beads by pulled still frame images from cMOS camera, quantity the position of individual beads, and compare their average positions from one image frame to the next. Based on this comparison, the software utilized programmed algorithms to determine whether the beads were moving toward (pDEP) or away from (nDEP) the edges of the IDEA fingers. This determination was used to automatically adjust the frequency so the analysis could be repeated.

Specifically, the program was designed to observe the beads within a specific "viewing window" which was set to encompass the gap between two fingers of the IDEA. Only Movement in the lateral direction, perpendicular to the electrode finger edges, was analyzed as this is the direction of the electric field lines, and as such, the DEP force. Based on the determination of particle movement, the system was designed to provide pre-programmed adjustment to the frequency of the applied AC bias. A visual representation of the top-level software architecture is provided in Figure 16. The following subsections detail specific aspects of this AI software program.

3.2.5 Bead Feature Detection and Extraction

OpenCV, a python package for image processing was used to capture and analyze still frame images from the camera's feed. For each frame, I_t, OpenCV's Hough Circle Detector function, which leverages the Hough Gradient Method to detect circular features within images, was utilized to detect the beads within the viewing window [85]. The parameters of this function were tuned; including Canny Detection Threshold, Center Detection Threshold, Minimum Radius, and Maximum Radius in order to improve the bead detection performance. The software stored detected beads in a python container denoted as B_t and the total number of detected beads was stored as variable N. The particle detection sub-loop is defined in the software as function F. Accordingly, the relation between each frame and the positional data of each detected particle can be represented as $F(I_t) = B_t = \{P_1, P_2, \ldots P_N\}$ where the variable P represents the 2 Dimensional coordinate of each detected bead.

From the extracted coordinate locations of each individual detected bead, the software then calculated the average absolute lateral distance of all detected bead (X_t) from the centerline of the view window which coincides with the center of the gap between each electrode finger. The absolute average distance from the centerline of this gap is used due to the fact that the gradient of DEP force is symmetric around this point. For example, a bead will be attracted to whichever electrode edge is closer when experiencing pDEP force. The function used for this calculation, denoted as G, is displayed as Equation 4 where x_n represents the lateral position of each individual detected bead and r represents the centerline of the electrode gap.

$$X_t = G(B_t) = \sum_{n=1}^{N} \left|\frac{x_n - r}{N}\right| \tag{4}$$

Equation 6: *Absolute Average Distance from Centerline Equation*

As such, the program converted each frame into a single numeric value of the average absolute distance from the center of the electrode gap of all detected beads. This value is subsequently used to evaluate if the beads are moving closer to or further from the edges of the electrodes, indicating the sign of the DEP force they are experiencing. This approach is referred to as quantifying the “bead bulk cloud behavior”.

3.2.6 Particle Movement Analysis

In order to assess the overall movement of the beads at each time interval *t*, the software was designed to perform a linear trend analysis (LTA) on the values of X_t for the frame under review and the previous 5 frames, a subset of the data stored as the variable *W* where $W = (X_t, X_{t-1}, X_{t-2}\ldots)$.

First, Python’s Data Smoothing function is used to perform linear convolution of subset *W,* to reduce the noise within the data and provide more defined trending during the LTA. After smoothing, the Linear Trend Model is executed using a least-squares regression to generate a linear trend line of each X_t value as a function of time, *t*. The slope of this trendline is store as variable b, which represents the velocity of the beads movement, and it’s sign represents the direction of bead movement.

The software then compares the velocity b to a threshold value, δ, to determine whether the particles are moving towards or away from the centerline of the electrode gap and thus, the sign of the DEP force the particle is experiencing. If $|b| < \delta$, it is determined no significant bead motion is occurring. In the case when $|b| > \delta$, bead motion is occurring, and the sign of DEP force takes on that of variable *b*.

3.2.7 Feedback Loop Control

The program was designed to send adjust commands for the frequency of the applied AC bias to the function generator based on the results from the Particle Movement Analysis sub-loop. The system stores the result of the movement analysis sub-loop as a state variable, *STATE*, which is either in a *No Movement*, *pDEP*, or *nDEP* state. After a pre-determine amount of time has elapsed, the program sends the adjustment command to the function generator. If *STATE* is defined as *pDEP* the frequency of the applied bias is increased and if defined as nDEP, the frequency is decreased. No adjustment is made when *STATE* is defined as *No Movement*, as this indicates the system has settled into the crossover frequency range.

3.3 Results and Discussion

3.3.1 Particle Detection

The cyber-physical system was setup and run as outlined in section 3.2. In addition to saving particle movement data, each still frame generated by the OpenCV package was saved for analysis. The cMOS camera was operated at a rate of 9 frames per second, thus every 9 frames represent one second of elapsed time. Figure 17 illustrates and example of a single still frame data point. The red portions of the frame are drawn by the AI program to denoted particles which have been successfully detected by the Hough Circle Function. The green portions, also drawn by the AI program, indicate the locate of the IDEA finger edge, thus establishing the software's viewing window across the electrode gap.

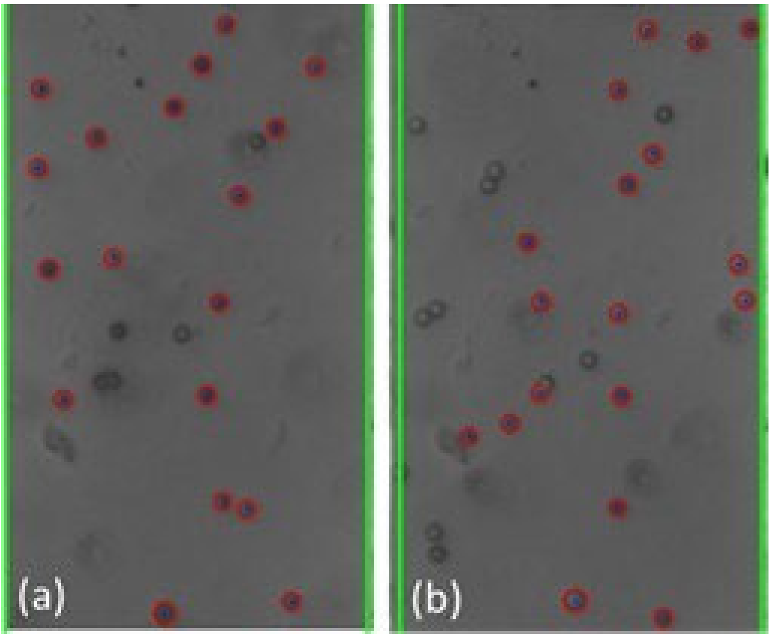

Figure 17: *Examples (a) and (b) of bead detection using The Hough Circle Detection function of the OpenCV package. The recognized beads are circled in red. The green lines identify the frame window nearly coincident with the edges of the electrodes.*

Based on assessment of each still frame data point collected by the software, the Hough Circle Function was successful at identifying an average of 20-30% of beads within each frame across multiple experimental runs. This rate of detection was determined to provide a sufficient sample size within each frame in order to accurately estimate average bead position and movement.

Experimentally, the efficacy of the bead detection sub-loop was found to depend on a handful of factors, including the illumination strength and optical focus of the microscope as well as the density and size of the beads. Generally, larger beads at lower concentrations lead to better bead detection. This is attributed to the fact that the Hough Circle Detector function uses pixel color gradient to extract circular features from an image, and thus larger beads provide a larger circumference over which the program can assess such gradients. Additionally, lower bead density within the viewing window lessened the propensity of the beads to form agglomerations, masking their circular geometry from the program. Detailed results pertaining to bead-to-bead interaction are presented in Section 3.3.5 below. Lastly, the contrast resulting from differing levels of illumination provided by the microscope affected the particle detection efficacy. Setting which increased the color contrast between the beads and the background silicon material provided for higher bead detection rates. Figure 18 demonstrates the impact bead size and image contrast had on bead detection.

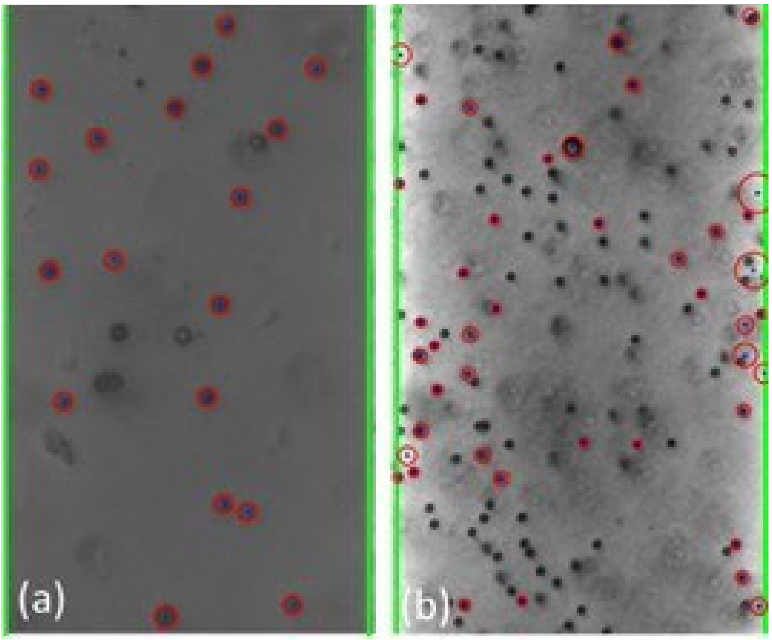

Figure 18: *Different bead detection efficacy between samples (a) and (b) depended on bead size and illumination conditions.*

3.3.2 Bulk Cloud Behavior

The cyber-physical system was setup and two trials were performed. For each trial, the program calculated the average absolute distance of all detected particles from the centerline of the electrode gap. This value was used to determine the bulk cloud behavior of the beads. The results of this calculation for each trial are presented in Figure 19 and Figure 20 below, overlaid with the changes to the frequency of the applied electric field.

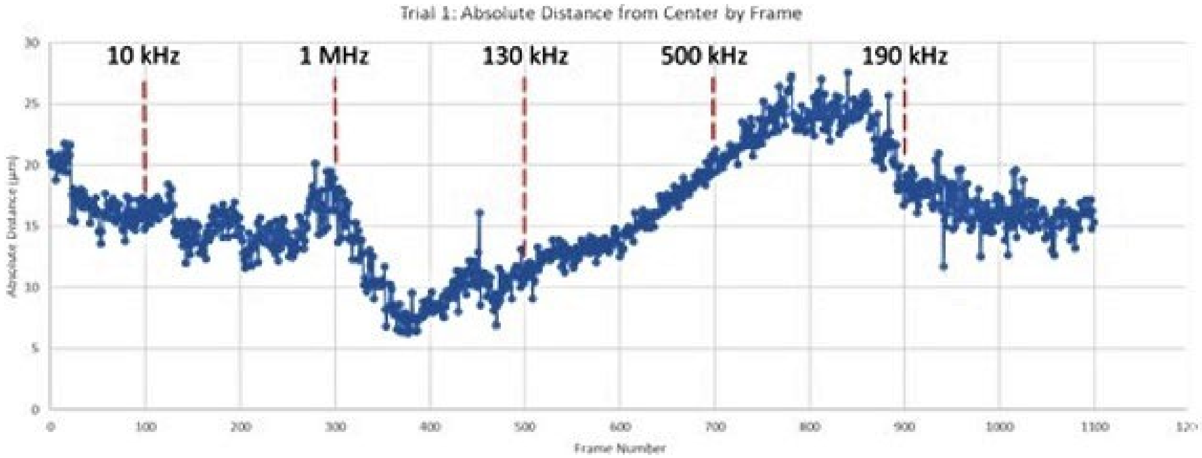

Figure 19: *Graphical Results from Trial 1.*

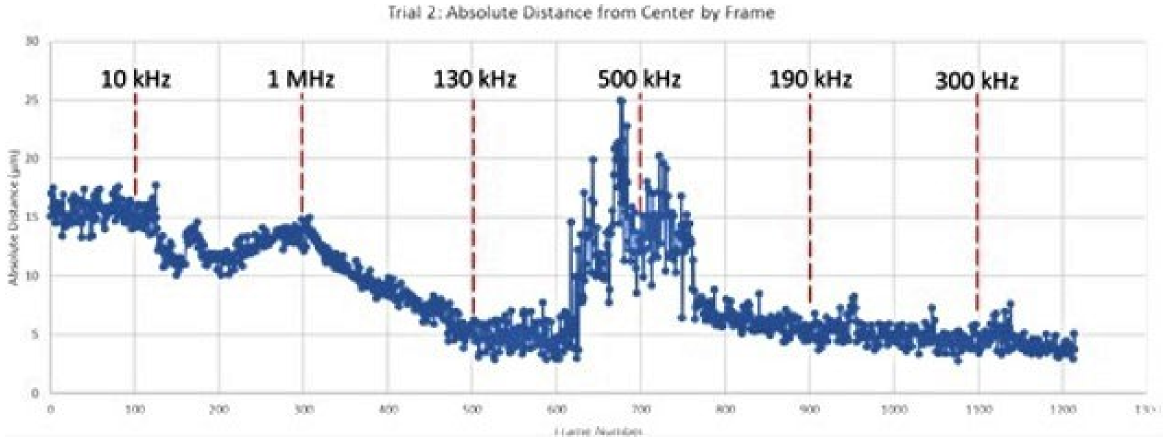

Figure 20: *Graphical Results from Trial 2*

For the given experimental setup, increasing absolute distance from the centerline is an indication that the particles are moving toward the edges of each electrode under the influence of pDEP. It should also be noted that this movement may also be the result of other attractive forces such as electroosmosis. Conversely, deceasing absolute distance from the centerline is indicative of nDEP force repelling the beads from the electrode edges. The results above depict clear regions of pDEP and nDEP force. One example from both trials is the change from 10 kHz to 1 MHz which resulted in a sharp decrease in the absolute distance as the beads experienced strong nDEP force. The frequency regions of attraction and repulsion within these results align with established literature on DEP force [86]. Furthermore it can be seen that as the frequency approached the crossover value and the magnitude of the DEP diminished, the magnitude of bead movement also decreased.

The results also indicate instances of delayed bead response to changes in the applied frequency. This is thought to be due to the beads residual momentum that must be overcome prior to a reversal in the direction of bead motion. This finding is important to understanding the fundamental physics of DEP-driven particle manipulation and this time delay must be accounted for in the design of software based systems for specific applications. Overall, across both trials, the cyber-physical system was found to be capable of using the average absolute distance to identify regions of pDEP and nDEP influence.

3.3.3 Individual Particle Behavior

In order to assess the change in movement at the individual bead level as a result of frequency adjustment, still frame images were analyzes from Trial 2 and are provided in the following figures. Select beads are highlighted within the images for clarity. This analysis confirms the beads were attracted to and repelled from the electrodes based on the applied frequency. For example, in Figure 21 beads are seen moving toward the electrode edges at an applied frequency of 10 kHz. The same beads can be seen moving away from the electrodes when the frequency is increased to 1 MHz in Figure 22.

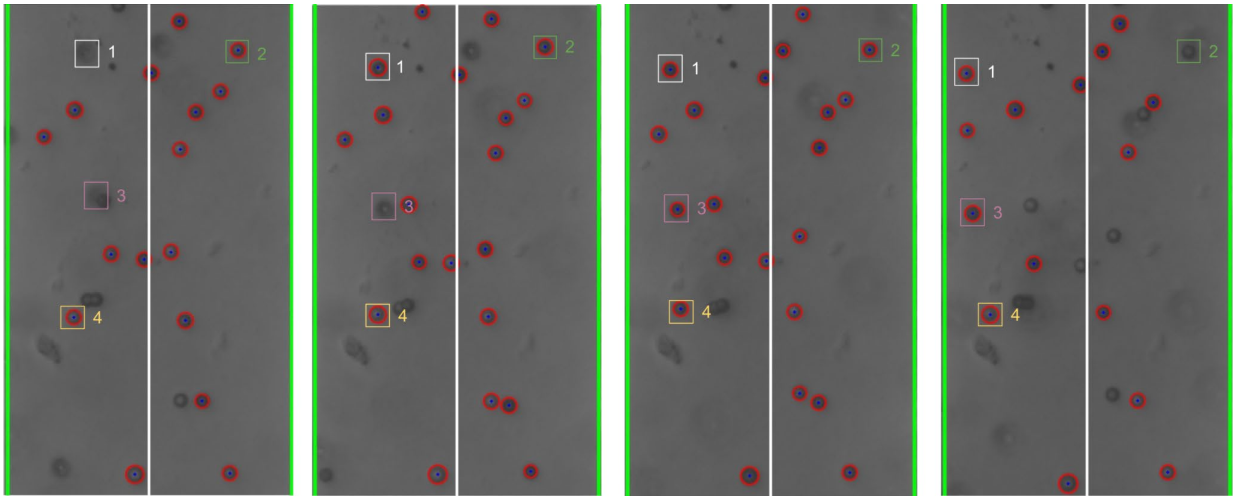

Figure 21: *Individual bead movement during Trial 2 from frames 195 to 298.*

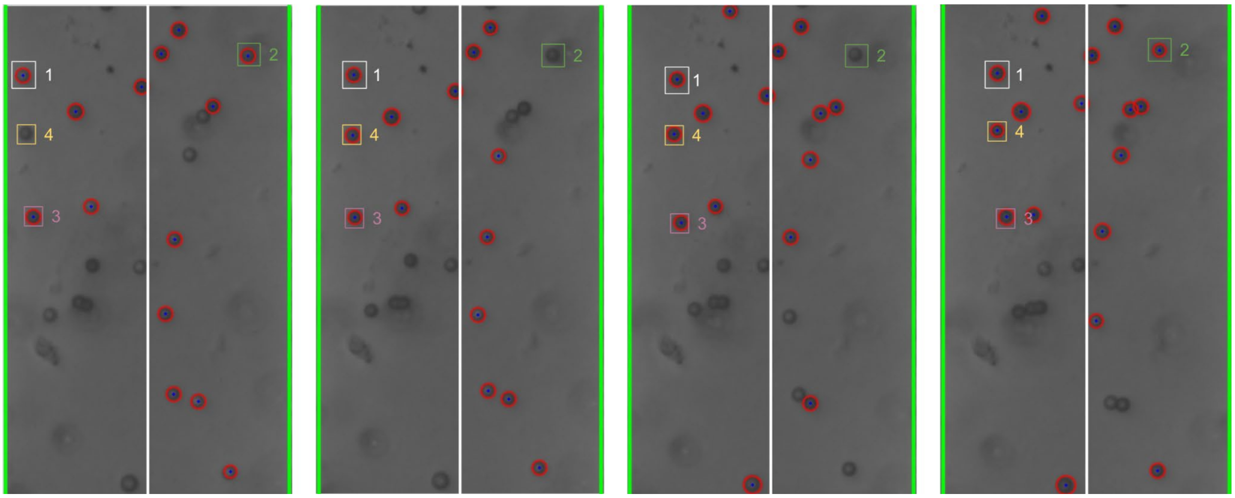

Figure 22: *Individual bead movement during Trial 2 from frames 300 to 340.*

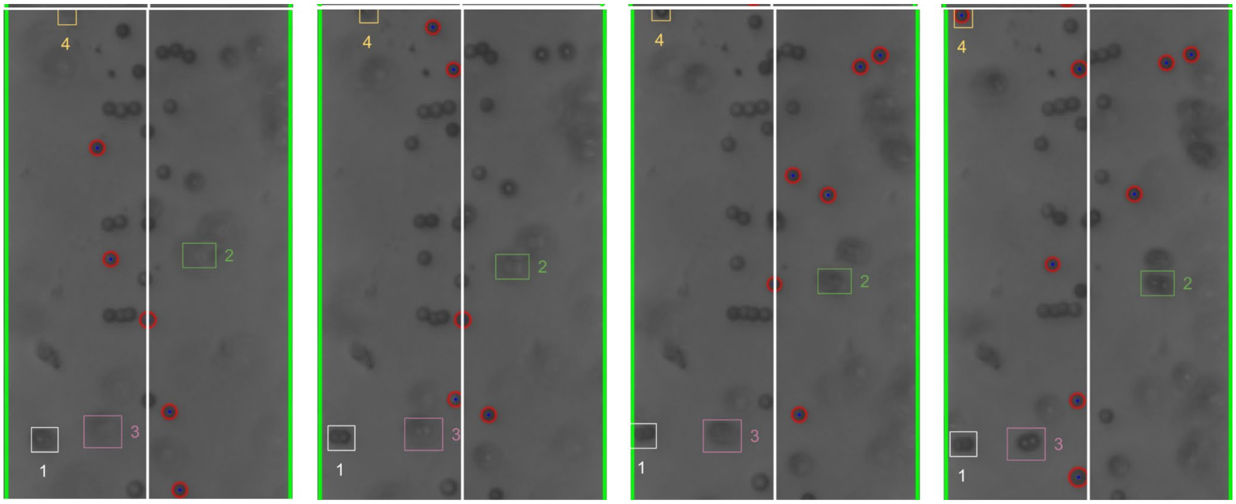

Figure 23: *Individual bead movement during Trial 2 from frames 570 to 685.*

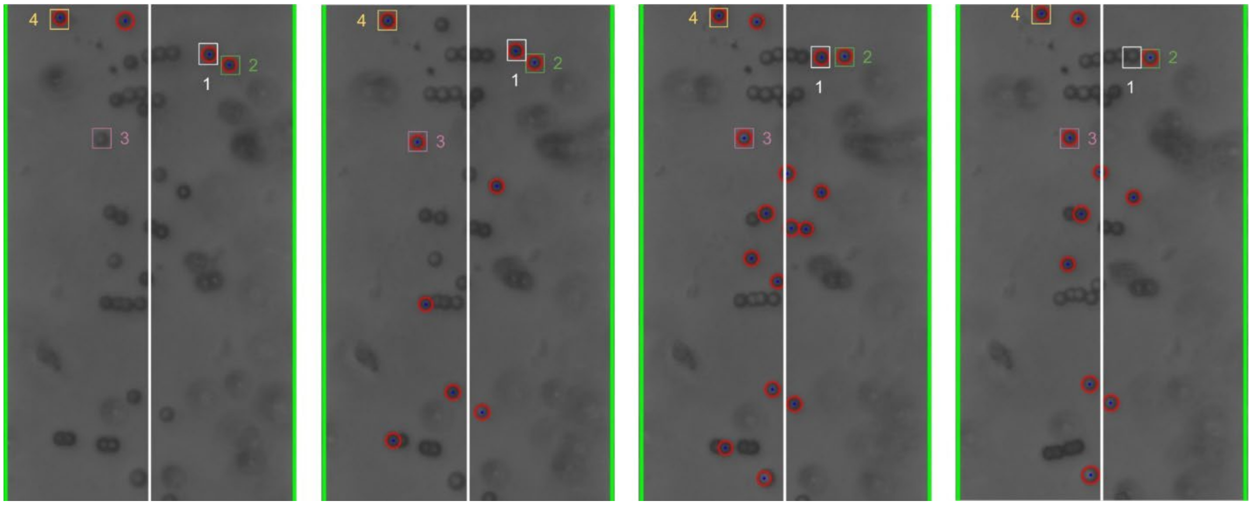

Figure 24: *Individual bead movement during Trial 2 from frames 735 to 812.*

3.3.4 Bulk Cloud vs. Individual Particle Behavior Comparison

When comparing the results from section 3.3.2 and section 3.3.3, it is found that the individual bead analysis correlates closely with the bulk bead behavior assessment made by the software program. For example, the steady decrease in the average absolute distance occurring at 1 MHz in trial 2 correlates well with the individual beads seen moving away from the electrodes in Figure 22.

These results support the assertion that the proposed AI based cyber-physical system is capable of effectively estimating the bead response to variable frequency input. The system successfully identified frequency regimes in which beads were attracted to the electrode surface due to pDEP and Electroosmosis as well as regimes in which they were repelled from the electrodes due to nDEP. As previously indicated, the results also revealed a time delay in particle movement attributed to residual bead momentum in relation to the strength of the DEP force at a given frequency. For example, in Trial 1 the beads response to increasing the frequency to 1 MHz at frame 300 was substantially quicker than when the frequency was changed to 500 kHz at Frame 700 in which a more gradual response is seen. This can be explained by the fact that the nDEP force at 1 MHz is substantially strong than at 500 kHz, and thus the beads' residual momentum is more quickly overcome, and their direction reversed.

In addition to estimating and quantifying frequency regimes of DEP influence, the program was also successful in estimating the system's crossover frequency. As the applied frequency approaches the theoretical crossover frequency, the DEP force acting on the beads becomes weaker, resulting in slower bead movement. Furthermore, the DEP force is strongest adjacent to the surface of the electrode and diminishes as the distance from the surface of the electrode increases. Thus, the further from the electrode a given bead is, the less force it will experience. This can be seen in the relative magnitude of bead motion in the still frame images in Figures 21-24 as well as the leveling off of average absolute distance from the centerline in Figure 19 and Figure 20. Based on the results generated by the program, the crossover frequency is estimated to be between 500kHz and 1 MHz. While the true crossover frequency for this system cannot be calculated as the conductivity of the CML modified polystyrene beads is not known, it is concluded that this estimate of the crossover frequency falls within the range determined by previous research using similar bead material [82-83].

The proposed cyber-physical system was successful at characterizing the regions of DEP influence, as well as the crossover frequency, across multiple trials. This supports the assertion that a phenomenological approach paired with AI is a viable method for estimating such regimes without the need for complex modeling or calculation. Bead-to-bead interaction and the formation of pearl chain structures which is detailed in the following section arose as a primary limiting factor in the system's ability to further refine these estimates.

3.3.5 Bead-to-Bead Interaction

Previous research has established that particles within a non-uniform electric field experience bead-to-bead attraction and form was is referred to as "pearl chains" along the electric field lines [87].

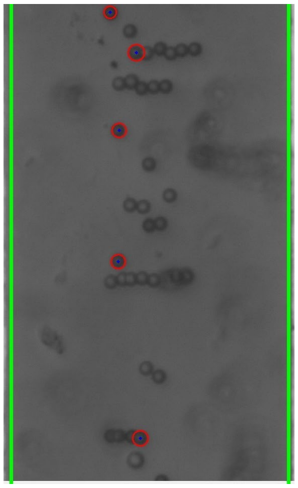

Figure 25: *Example of Pearl Chain Formation*

This phenomenon was demonstrated by the beads within these experiments and the pearl chains can be seen in the still frame images such as the one in Figure 25. The formation of these pearl chains impact the response of the beads to DEP force. As the chains grow, their movement is stunted by increasing drag force and inertia. Additionally, the formation of these chains prohibits the Hough Circle Detector function within the software from identifying the beads by distorting the color gradient used to detect the edge of the beads. This is demonstrated in Figure 25 which shows that none of the beads in the pearl chains are detected by the software.

3.4 Chapter Summary

The cyber-physical system presented in this research successfully implemented algorithmic artificial intelligence and a phenomenological approach to characterize particle response to varying frequency of an applied electric field. As described in the previous sections, the system was capable of identifying frequency regimes of pDEP/EO and nDEP force as well as regimes of weak DEP force, including the crossover frequency range. This research serves as a first proof of concept that artificial intelligence can be used to study the complex forces exerted on objects in the micro domain. Such integration of AI may help to further enhance current microfabrication techniques, specifically parallel bottom-up assembly and may find application in a variety of fields including drug-delivery, microsensors and bioassays. Additionally, the proposed system's phenomenological approach is well suited to assess system in which the plurality and/or complexity of the system makes modelling or calculation prohibitive. The system represents a singular tool for the study and characterization of a variety of systems, which speaks to the time and cost advantages of implementing AI in microfabrication methods and research.

Chapter 4 – Conclusion

Continued development of miniaturization processes and capabilities will play a critical role in the further advancement of modern technology. From the computing, electronics, and telecommunications industries to healthcare and biotechnology, miniaturization represents an exciting new frontier and an opportunity to capitalize on the benefits that come with designing and operating devices in the micro and nano domains. Furthermore, miniaturization may serve as an important tool in combating serious challenges facing society today. The global climate change crisis is placing increasing pressure to reduce the world's power consumption, requiring new technologies that operate more efficiently with less energy input. Furthermore, rapid depletion of finite natural resources, such as metals and fossil fuels from which most plastic materials are derived, will require reduction in the material requirements to manufacture the world's products and a drastic reduction of waste.

In order for miniaturization to serve as a pathway to solve these challenges, further research and development into micro and nano manufacturing processes is vital. In particular, establishment of micro assembly techniques which are capable of high throughput and operation at low cost will play a key role in bringing micro manufacturing to industrial scale in a commercially viable way.

The electrokinetically driven parallel assembly process presented in Chapter 2 serves as a strong proof of concept and example of the utility of such processes to create micro structures and devices that address real-world problems. The advantages of these parallel assembly techniques become obvious when their speed, ease of use, and relative low cost are compared to established pick-and-place methods. Further research into the application of electrokinetically driven micro-object assembly, sorting, and manipulation, particularly of biological material, is of particular interest. Specifically, assembly of CNT bridges such as those presented in this study across damages in neurologic systems within the human body to treat spinal cord and other nervous system damage is an exciting prospect that warrants additional attention.

Further development of these parallel assembly techniques will require new technologies and approaches in order to overcome the challenges that come along with operating in the micro and nano domain. The forces that act on objects within the micro and nano domain are multiple and complex, even in the simplest of systems. The traditional approach to characterizing and calculating these forces and modelling the response of micro objects to them will quickly become a limiting factor in the advancement of parallel assembly techniques.

The research presented in Chapter 3 introduces a novel phenomenological approach to this characterization and response prediction, aided by use of artificial intelligence. The cyber-physical system presented in this research successfully characterized the response of polystyrene beads to dielectrophoretic force without the need for complex modeling and careful characterization of the material, chemical, and electrical properties of the beads or medium. Further development of such technologies will dramatically improve the ability to research and design parallel micro assembly techniques, even as systems of interest become increasingly complex.

The design of the detailed cyber-physical system relies on algorithm artificial intelligence. However, the use of more advanced machine learning technologies, for example neural networks, is an interesting and exciting prospect which may further build upon this research to establish systems capable of more precise and comprehensive characterization of these complex micro domain forces.

This work seeks to contribute to a young, but rapidly progressing era in micromanufacturing. While Micromanufacturing is a well-established field of study, recent advancements in our understanding of the micro and nano domain, paired with the new tools and technologies at researchers’ disposal, such as artificial intelligence, is ushering in a revitalized effort to push our modern technology forward by shrinking it down to the micro and nano length scales.

References

1. Frazier, A. B., Warrington, R. O., & Friedrich, C. (1995). The miniaturization technologies: Past, present, and future. *IEEE Transactions on Industrial Electronics*, *42*(5), 423–430. https://doi.org/10.1109/41.464603

2. Brinkman, W. F., Haggan, D. E., & Troutman, W. W. (1997). A history of the invention of the transistor and where it will lead us. *IEEE Journal of Solid-State Circuits*, *32*(12), 1858–1865. https://doi.org/10.1109/4.643644

3. Early, J. M. (2001). Out to Murray Hill to play: An early history of transistors. *IEEE Transactions on Electron Devices*, *48*(11), 2468–2472. https://doi.org/10.1109/16.960369

4. Wang, P., Lu, Q., & Fan, Z. (2019). Evolutionary design optimization of MEMS: A review of its history and state-of-the-art. *Cluster Computing*, *22*(S4), 9105–9111. https://doi.org/10.1007/s10586-018-2085-3

5. Madou, M. J. (2018). *Fundamentals of microfabrication: The science of miniaturization, second edition*. CRC Press.

6. Kricka, L. J. (1998). Miniaturization of analytical systems. *Clinical Chemistry*, *44*(9), 2008–2014. https://doi.org/10.1093/clinchem/44.9.2008

7. Judy, J. W. (2001). Microelectromechanical systems (Mems): Fabrication, design and applications. *Smart Materials and Structures*, *10*(6), 1115–1134. https://doi.org/10.1088/0964-1726/10/6/301

8. Qin, Y., Brockett, A., Ma, Y., Razali, A., Zhao, J., Harrison, C., Pan, W., Dai, X., & Loziak, D. (2010). Micro-manufacturing: Research, technology outcomes and development issues. *The International Journal of Advanced Manufacturing Technology*, *47*(9–12), 821–837. https://doi.org/10.1007/s00170-009-2411-2

9. Fassi, I., & Shipley, D. (Eds.). (2017). *Micro-manufacturing technologies and their applications: A theoretical and practical guide*. Springer International Publishing. https://doi.org/10.1007/978-3-319-39651-4

10. Razali, A. R., & Qin, Y. (2013). A review on micro-manufacturing, micro-forming and their key issues. *Procedia Engineering*, *53*, 665–672. https://doi.org/10.1016/j.proeng.2013.02.086

11. Wich, T., Edeler, C., Stolle, C., & Fatikow, S. (2009). Micro-nano-integration based on automated serial assembly. *2009 IEEE International Conference on Automation Science and Engineering*, 573–578. https://doi.org/10.1109/COASE.2009.5234150

12. Kim, C.-J., Pisano, A. P., & Muller, R. S. (1992). Silicon-processed overhanging microgripper. *Journal of Microelectromechanical Systems*, *1*(1), 31–36. https://doi.org/10.1109/84.128053

13. Nah, S. K., & Zhong, Z. W. (2007). A microgripper using piezoelectric actuation for micro-object manipulation. *Sensors and Actuators A: Physical*, *133*(1), 218–224. https://doi.org/10.1016/j.sna.2006.03.014

14. Chu, P. B., & Pister, S. J. (1994). Analysis of closed-loop control of parallel-plate electrostatic microgrippers. *Proceedings of the 1994 IEEE International Conference on Robotics and Automation*, 820–825. https://doi.org/10.1109/ROBOT.1994.351387

15. Mehrabi, H., & Aminzahed, I. (2020). Design and testing of a microgripper with SMA actuator for manipulation of micro components. *Microsystem Technologies*, *26*(2), 531–536. https://doi.org/10.1007/s00542-019-04523-y

16. Beyeler, F., Bell, D. J., Nelson, B. J., Sun, Y., Neild, A., Oberti, S., & Dual, J. (2006). Design of a micro-gripper and an ultrasonic manipulator for handling micron sized objects. *2006 IEEE/RSJ International Conference on Intelligent Robots and Systems*, 772–777. https://doi.org/10.1109/IROS.2006.282628

17. Lambert, P., Seigneur, F., Chollet, S., & Jacot, J. (2006). Design of a capillary gripper for a submillimetric application. *IPAS*. https://doi.org/10.1007/0-387-31277-3_1

18. Tai, K., El-Sayed, A.-R., Shahriari, M., Biglarbegian, M., & Mahmud, S. (2016). State of the art robotic grippers and applications. *Robotics*, *5*(2), 11. https://doi.org/10.3390/robotics5020011

19. Heriban, D., & Gauthier, M. (2008). Robotic micro-assembly of microparts using a piezogripper. *2008 IEEE/RSJ International Conference on Intelligent Robots and Systems*, 4042–4047. https://doi.org/10.1109/IROS.2008.4650932

20. Tasoglu, S., Yu, C. H., Gungordu, H. I., Guven, S., Vural, T., & Demirci, U. (2014). Guided and magnetic self-assembly of tunable magnetoceptive gels. *Nature Communications*, *5*(1), 4702. https://doi.org/10.1038/ncomms5702

21. Steager, E. B., Sakar, M. S., Kim, D. H., Kumar, V., Pappas, G. J., & Kim, M. J. (2011). Electrokinetic and optical control of bacterial microrobots. *Journal of Micromechanics and Microengineering*, *21*(3), 035001. https://doi.org/10.1088/0960-1317/21/3/035001

22. Zhou, T., Chen, J., Kropp, E., & Kulinsky, L. (2020). Guided electrokinetic assembly of polystyrene microbeads onto photopatterned carbon electrode arrays. *ACS Applied Materials & Interfaces*, *12*(31), 35647–35656. https://doi.org/10.1021/acsami.0c08266

23. Zhou, T., Michaels, M., & Kulinsky, L. (2021). Guided healing of damaged microelectrodes via electrokinetic assembly of conductive carbon nanotube bridges. *Micromachines*, *12*(4), 405. https://doi.org/10.3390/mi12040405

24. Michaels, M., Yu, S.-Y., Zhou, T., Du, F., Al Faruque, M. A., & Kulinsky, L. (2022). Artificial intelligence algorithms enable automated characterization of the positive and negative dielectrophoretic ranges of applied frequency. *Micromachines*, *13*(3), 399. https://doi.org/10.3390/mi13030399
25. Hu, J., Wang, Y., Li, D., & Cheng, Y.-T. (2018). Effects of adhesion and cohesion on the electrochemical performance and durability of silicon composite electrodes. *Journal of Power Sources*, *397*, 223–230. https://doi.org/10.1016/j.jpowsour.2018.06.103

26. Xu, W., Huang, L.-B., & Hao, J. (2017). Fully self-healing and shape-tailorable triboelectric nanogenerators based on healable polymer and magnetic-assisted electrode. *Nano Energy*, *40*, 399–407. https://doi.org/10.1016/j.nanoen.2017.08.045

27. Chen, J., Yang, J., Guo, H., Li, Z., Zheng, L., Su, Y., Wen, Z., Fan, X., & Wang, Z. L. (2015). Automatic mode transition enabled robust triboelectric nanogenerators. *ACS Nano*, *9*(12), 12334–12343. https://doi.org/10.1021/acsnano.5b05618

28. Tahir, M., He, L., Yang, W., Hong, X., Haider, W. A., Tang, H., Zhu, Z., Owusu, K. A., & Mai, L. (2020). Boosting the electrochemical performance and reliability of conducting polymer microelectrode via intermediate graphene for on-chip asymmetric micro-supercapacitor. *Journal of Energy Chemistry*, *49*, 224–232. https://doi.org/10.1016/j.jechem.2020.02.036

29. Zhu, X., Xie, Y., Chen, H., & Luan, W. (2021). Numerical analysis of the cyclic mechanical damage of Li-ion battery electrode and experimental validation. *International Journal of Fatigue*, *142*, 105915. https://doi.org/10.1016/j.ijfatigue.2020.105915

30. Yang, S., Feng, X., Ivanovici, S., & Müllen, K. (2010). Fabrication of graphene-encapsulated oxide nanoparticles: Towards high-performance anode materials for lithium storage. *Angewandte Chemie International Edition*, *49*(45), 8408–8411. https://doi.org/10.1002/anie.201003485

31. Usui, H., Wasada, K., Shimizu, M., & Sakaguchi, H. (2013). TiO2/Si composites synthesized by sol–gel method and their improved electrode performance as Li-ion battery anodes. *Electrochimica Acta*, *111*, 575–580. https://doi.org/10.1016/j.electacta.2013.08.015

32. Wang, C., Wu, H., Chen, Z., McDowell, M. T., Cui, Y., & Bao, Z. (2013). Self-healing chemistry enables the stable operation of silicon microparticle anodes for high-energy lithium-ion batteries. *Nature Chemistry*, *5*(12), 1042–1048. https://doi.org/10.1038/nchem.1802

33. Sim, H. J., Kim, H., Jang, Y., Spinks, G. M., Gambhir, S., Officer, D. L., Wallace, G. G., & Kim, S. J. (2019). Self-healing electrode with high electrical conductivity and mechanical strength for artificial electronic skin. *ACS Applied Materials & Interfaces*, *11*(49), 46026–46033. https://doi.org/10.1021/acsami.9b10100

34. Wang, Y., Su, Y., Wang, Z., Zhang, Z., Han, X., Dong, M., Cui, L., & Chen, M. (2018). Reversible conductivity recovery of highly sensitive flexible devices by water vapor. *Npj Flexible Electronics*, *2*(1), 31. https://doi.org/10.1038/s41528-018-0043-z

35. Liu, Y., Gao, M., Mei, S., Han, Y., & Liu, J. (2013). Ultra-compliant liquid metal electrodes with in-plane self-healing capability for dielectric elastomer actuators. *Applied Physics Letters*, *103*(6), 064101. https://doi.org/10.1063/1.4817977

36. Wu, C., Tang, X., Gan, L., Li, W., Zhang, J., Wang, H., Qin, Z., Zhang, T., Zhou, T., Huang, J., Xie, C., & Zeng, D. (2019). High-adhesion stretchable electrode via cross-linking intensified electroless deposition on a biomimetic elastomeric micropore film. *ACS Applied Materials & Interfaces*, *11*(22), 20535–20544. https://doi.org/10.1021/acsami.9b05135

37. Iijima, S. (1991). Helical microtubules of graphitic carbon. *Nature*, *354*(6348), 56–58. https://doi.org/10.1038/354056a0

38. Haddon, R. C. (2002). Carbon nanotubes. *Accounts of Chemical Research*, *35*(12), 997–997. https://doi.org/10.1021/ar020259h

39. De Volder, M. F. L., Tawfick, S. H., Baughman, R. H., & Hart, A. J. (2013). Carbon nanotubes: Present and future commercial applications. *Science*, *339*(6119), 535–539. https://doi.org/10.1126/science.1222453

40. Chen, X. Q., Saito, T., Yamada, H., & Matsushige, K. (2001). Aligning single-wall carbon nanotubes with an alternating-current electric field. *Applied Physics Letters*, *78*(23), 3714–3716. https://doi.org/10.1063/1.1377627

41. Perez-Gonzalez, V. H., Ho, V., Vazquez-Pinon, M., Martinez-Chapa, S. O., & Kulinsky, L. (2015). A novel micro/nano fabrication process based on the combined use of dielectrophoresis, electroosmotic flow, and electrodeposition for surface patterning. *Journal of Micromechanics and Microengineering*, *25*(11), 115007. https://doi.org/10.1088/0960-1317/25/11/115007

42. Ramos, A., Morgan, H., Green, N. G., & Castellanos, A. (1998). Ac electrokinetics: A review of forces in microelectrode structures. *Journal of Physics D: Applied Physics*, *31*(18), 2338–2353. https://doi.org/10.1088/0022-3727/31/18/021

43. Seo, H.-W., Han, C.-S., Choi, D.-G., Kim, K.-S., & Lee, Y.-H. (2005). Controlled assembly of single SWNTs bundle using dielectrophoresis. *Microelectronic Engineering*, *81*(1), 83–89. https://doi.org/10.1016/j.mee.2005.04.001

44. Kendall, K. (1996). Electromechanics of particles. *Powder Technology*, *2*(89), 177-178.

45. Dimaki, M., & Bøggild, P. (2004). Dielectrophoresis of carbon nanotubes using microelectrodes: A numerical study. *Nanotechnology*, *15*(8), 1095–1102. https://doi.org/10.1088/0957-4484/15/8/039

46. Katz, D., Lopez, D., Kornblit, A., & Grebel, H. (2008). Carbon nanotubes bridges spanning across metal electrode tips. *Journal of nanoscience and nanotechnology*, *8*(9), 4382–4386.

47. Li, J., Ye, Q., Cassell, A., Ng, H. T., Stevens, R., Han, J., & Meyyappan, M. (2003). Bottom-up approach for carbon nanotube interconnects. *Applied Physics Letters*, *82*(15), 2491–2493. https://doi.org/10.1063/1.1566791

48. Todri-Sanial, A. (2016). *Carbon nanotubes for interconnects*. Springer Science+Business Media.

49. Hällström, W., Prinz, C. N., Suyatin, D., Samuelson, L., Montelius, L., & Kanje, M. (2009). Rectifying and sorting of regenerating axons by free-standing nanowire patterns: A highway for nerve fibers. *Langmuir*, *25*(8), 4343–4346. https://doi.org/10.1021/la900436e

50. You, R., Zhang, Q., Li, X., Yan, S., Luo, Z., Qu, J., & Li, M. (2020). Multichannel bioactive silk nanofiber conduits direct and enhance axonal regeneration after spinal cord injury. *ACS Biomaterials Science & Engineering*, *6*(8), 4677–4686. https://doi.org/10.1021/acsbiomaterials.0c00698

51. Li, X., Zhang, C., Haggerty, A. E., Yan, J., Lan, M., Seu, M., Yang, M., Marlow, M. M., Maldonado-Lasunción, I., Cho, B., Zhou, Z., Chen, L., Martin, R., Nitobe, Y., Yamane, K., You, H., Reddy, S., Quan, D.-P., Oudega, M., & Mao, H.-Q. (2020). The effect of a nanofiber-hydrogel composite on neural tissue repair and regeneration in the contused spinal cord. *Biomaterials*, *245*, 119978. https://doi.org/10.1016/j.biomaterials.2020.119978

52. Schönenberger, C., Bachtold, A., Strunk, C., Salvetat, J.-P., & Forró, L. (1999). Interference and Interaction in multi-wall carbon nanotubes. *Applied Physics A: Materials Science & Processing*, *69*(3), 283–295. https://doi.org/10.1007/s003390051003

53. Seiphoori, A., Ma, X., Arratia, P. E., & Jerolmack, D. J. (2020). Formation of stable aggregates by fluid-assembled solid bridges. *Proceedings of the National Academy of Sciences*, *117*(7), 3375–3381. https://doi.org/10.1073/pnas.1913855117

54. Schmitt, R. (2002). *Electromagnetics explained: A handbook for wireless/RF, EMC, and high-speed electronics*. Newnes.

55. Huang, Y., Huang, Y., Zhu, M., Meng, W., Pei, Z., Liu, C., Hu, H., & Zhi, C. (2015). Magnetic-assisted, self-healable, yarn-based supercapacitor. *ACS Nano*, *9*(6), 6242–6251. https://doi.org/10.1021/acsnano.5b01602

56. Huynh, T., Sonar, P., & Haick, H. (2017). Advanced materials for use in soft self-healing devices. *Advanced Materials*, *29*(19), 1604973. https://doi.org/10.1002/adma.201604973

57. Michel, S., Chu, B. T. T., Grimm, S., Nüesch, F. A., Borgschulte, A., & Opris, D. M. (2012). Self-healing electrodes for dielectric elastomer actuators. *Journal of Materials Chemistry*, *22*(38), 20736. https://doi.org/10.1039/c2jm32228e

58. Lee, J.-O., Park, C., Kim, J.-J., Kim, J., Park, J. W., & Yoo, K.-H. (2000). Formation of low-resistance ohmic contacts between carbon nanotube and metal electrodes by a rapid thermal annealing method. *Journal of Physics D: Applied Physics*, *33*(16), 1953–1956. https://doi.org/10.1088/0022-3727/33/16/303

59. Tan, Y. J., Wu, J., Li, H., & Tee, B. C. K. (2018). Self-healing electronic materials for a smart and sustainable future. *ACS Applied Materials & Interfaces*, *10*(18), 15331–15345. https://doi.org/10.1021/acsami.7b19511

60. Rosso, K. M., & Zarzycki, P. (2021). The steady march toward biomimetic nanoelectronics. *ACS Nano*, *15*(5), 7844–7847. https://doi.org/10.1021/acsnano.1c01923

61. Ariga, K. (2021). Nanoarchitectonics: What's coming next after nanotechnology? *Nanoscale Horizons*, *6*(5), 364–378. https://doi.org/10.1039/D0NH00680G

62. Pramanik, P. K. D., Solanki, A., Debnath, A., Nayyar, A., El-Sappagh, S., & Kwak, K.-S. (2020). Advancing modern healthcare with nanotechnology, nanobiosensors, and internet of nano things: Taxonomies, applications, architecture, and challenges. *IEEE Access*, *8*, 65230–65266. https://doi.org/10.1109/ACCESS.2020.2984269

63. Silva, T. C., Eppink, M., & Ottens, M. (2021). Automation and miniaturization: Enabling tools for fast, high-throughput process development in integrated continuous biomanufacturing. *Journal of Chemical Technology & Biotechnology*, jctb.6792. https://doi.org/10.1002/jctb.6792

64. Ruggeri, S. (2017). *Micro-manufacturing technologies and their applications*. Springer Berlin Heidelberg.

65. Cohn, M. B., Boehringer, K. F., & Noworolski, J. M. (1998). Microassembly Technologies for MEMS. *SPIE*, *Microelectronic Structures and MEMS for Optical Processing IV*, 2–16.

66. Keller, C. (1998, May 10). Microgrippers with integrated actuators and force sensors. *Proceedings of the World Automation Congress*.

67. Dechev, N., Cleghorn, W. L., & Mills, J. K. (2003). Microassembly of 3D MEMS structures utilizing a MEMS microgripper with a robotic manipulator. *2003 IEEE International Conference on Robotics and Automation (Cat. No.03CH37422)*, *3*, 3193–3199.

68. Kim, E., Kojima, M., Mae, Y., & Arai, T. (2020). High-speed manipulation of microobjects using an automated two-fingered microhand for 3d microassembly. *Micromachines*, *11*(5), 534. https://doi.org/10.3390/mi11050534

69. Lambert, P. (2007). *Capillary forces in microassembly: Modeling, simulation, experiments, and case study*. Springer Science+Business Media, LLC Springer e-books.

70. Liu, X., Shi, Q., Lin, Y., Kojima, M., Mae, Y., Huang, Q., Fukuda, T., & Arai, T. (2018). Hydrodynamic tweezers: Trapping and transportation in microscale using vortex induced by oscillation of a single piezoelectric actuator. *Sensors*, *18*(7), 2002. https://doi.org/10.3390/s18072002

71. Zhang, Z., Wang, X., Liu, J., Dai, C., & Sun, Y. (2019). Robotic micromanipulation: Fundamentals and applications. *Annual Review of Control, Robotics, and Autonomous Systems*, *2*(1), 181–203. https://doi.org/10.1146/annurev-control-053018-023755

72. Dou, Y., Wang, B., Jin, M., Yu, Y., Zhou, G., & Shui, L. (2017). A review on self-assembly in microfluidic devices. *Journal of Micromechanics and Microengineering*, *27*(11), 113002. https://doi.org/10.1088/1361-6439/aa84db

73. Zhang, H., Cadusch, J., Kinnear, C., James, T., Roberts, A., & Mulvaney, P. (2018). Direct assembly of large area nanoparticle arrays. *ACS Nano*, *12*(8), 7529–7537. https://doi.org/10.1021/acsnano.8b02932

74. Jia, S., Wang, J., Xie, M., Sun, J., Liu, H., Zhang, Y., Chao, J., Li, J., Wang, L., Lin, J., Gothelf, K. V., & Fan, C. (2019). Programming DNA origami patterning with non-canonical DNA-based metallization reactions. *Nature Communications*, *10*(1), 5597. https://doi.org/10.1038/s41467-019-13507-5

75. Gabler, F., Karnaushenko, D. D., Karnaushenko, D., & Schmidt, O. G. (2019). Magnetic origami creates high performance micro devices. *Nature Communications*, *10*(1), 3013. https://doi.org/10.1038/s41467-019-10947-x

76. Jones, T. B. (2003). Basic theory of dielectrophoresis and electrorotation. *IEEE Engineering in Medicine and Biology Magazine*, *22*(6), 33–42. https://doi.org/10.1109/MEMB.2003.1304999

77. Gascoyne, P. R. C., & Vykoukal, J. (2002). Particle separation by dielectrophoresis. *ELECTROPHORESIS*, *23*(13), 1973. https://doi.org/10.1002/1522-2683(200207)23:13<1973::AID-ELPS1973>3.0.CO;2-1

78. Li, Y., Dalton, C., Crabtree, H. J., Nilsson, G., & Kaler, K. V. I. S. (2007). Continuous dielectrophoretic cell separation microfluidic device. *Lab on a Chip*, *7*(2), 239–248. https://doi.org/10.1039/B613344D

79. Han, S.-I., Huang, C., & Han, A. (2020). In-droplet cell separation based on bipolar dielectrophoretic response to facilitate cellular droplet assays. *Lab on a Chip*, *20*(20), 3832–3841. https://doi.org/10.1039/D0LC00710B

80. Turcan, I., & Olariu, M. A. (2020). Dielectrophoretic manipulation of cancer cells and their electrical characterization. *ACS Combinatorial Science*, *22*(11), 554–578. https://doi.org/10.1021/acscombsci.0c00109

81. Gascoyne, P., & Shim, S. (2014). Isolation of circulating tumor cells by dielectrophoresis. *Cancers*, *6*(1), 545–579. https://doi.org/10.3390/cancers6010545

82. Inaba, M., Hayashi, S., Li, H., Kamimura, M., Nakano, M., & Suehiro, J. (2020). Dielectrophoretic properties of submicron diamond particles in sodium chloride aqueous solution. *Japanese Journal of Applied Physics*, *59*(4), 046502. https://doi.org/10.35848/1347-4065/ab7baf

83. Yafouz, B., Kadri, N., & Ibrahim, F. (2014). Dielectrophoretic manipulation and separation of microparticles using microarray dot electrodes. *Sensors*, *14*(4), 6356–6369. https://doi.org/10.3390/s140406356

84. Chen, Q., & Yuan, Y. J. (2019). A review of polystyrene bead manipulation by dielectrophoresis. *RSC Advances*, *9*(9), 4963–4981. https://doi.org/10.1039/C8RA09017C

85. Brahmbhatt, S. (2013). *Practical opencv*. Apress.

86. Sarno, B., Heineck, D., Heller, M. J., & Ibsen, S. D. (2021). Dielectrophoresis: Developments and applications from 2010 to 2020. *ELECTROPHORESIS*, *42*(5), 539–564. https://doi.org/10.1002/elps.202000156

87. Ding, H., Liu, W., Ding, Y., Shao, J., Zhang, L., Liu, P., & Liu, H. (2014). Particle clustering during pearl chain formation in a conductive-island based dielectrophoretic assembly system. *RSC Advances*, *5*(8), 5523–5532. https://doi.org/10.1039/C4RA10721G